UNIVERSITÀ DEGLI STUDI DI PADOVA

Dipartimento di Fisica e Astronomia "Galileo Galilei"

Master Degree in Physics

Final Dissertation

Detector and readout studies (experimental tests and simulation) for neutron and gamma detection

Thesis supervisor

Prof. Sandra Moretto

Thesis co-supervisor

Dr. Felix Pino

Candidate

Omar Nasr

Academic Year 2021/2022

Abstract

Nowadays, the applications for nuclear physics have become abundant which paved the way to more intensive and directed research in the field of nuclear detectors. Two example for these applications are the DRAGoN (Drone for Radiation detection of Gammas and Neutrons) project which aims to develop a compact detection system that can fit on an unmanned drone, and the active target of SPES (Selective Production of Exotic Species) project which aims to study fundamental nuclear physics and astrophysics.

In this work, characterisation of an organic detector (EJ-276G) was done to obtain the light output function of the scintillator. Furthermore, the characterization and comparison between the performance of the same scintillator coupled with a novel scintillation material for thermal neutron detection serves the purpose of determining the possibility of this material's use for the DRAGoN project which requires fast and thermal neutron detection in addition to the gamma detection. The setup was tested with a PMT and an SiPM to compare the performance in both cases. Simulation was made to determine the efficiency of the scintillator using Californium source to compare with the experimental efficiency.

Finally, a characterisation of a relatively new inorganic crystal was made from Strontium Iodide was made using PMT and SiPM to determine its energy resolution using different setups to assess the possibility of its use for the DRAGoN project or for secondary detection system for an experiment of SPES.

Acknowledgment

The completion of my thesis could not have been done without the help and care of many people. Firstly, I would like to thank my supervisors Prof. Sandra and Dr. Felix for all their help and guidance despite all the circumstances that took place and all the lessons I learned I take to heart to guide me through my academic life. Additionally, I want to thank the Erasmus Mundus Nucphys program for providing me with opportunity to learn so many things, meet wonderful people, and integrating me and so many others into the the wonderful community of nuclear physics.

I want to thank my amazing and loving family for all the support and love they always give me as their love and prayers are what kept me going throughout my life. They are the reason behind the success and happiness in my life. I love you to the expanding edge of the universe and back.

Finally, I would like to thank my true friends from Egypt who helped me and supported me emotionally, and academically throughout the years and I want thank all my Erasmus friends for being my family abroad and helping me through tough times. I wish you all the best in life and may our paths remain intertwined forever.

Contents

List of Figures

List of Tables

List of acronyms

FNGT	Fast Neutron and Gamma Transmission
DRAGoN	Drone for Radiation detection of Gammas and Neutrons
SPES	Selective Production of Exotic Species
RIB	Radioactive Ion Beam
AcTar	Active Target
TPC	Time Projection Chamber
PMT	Photomultiplier
CsI(Tl)	Thallium doped Cesium Iodide
NaI(Tl)	Sodium doped Cesium Iodide
CLLB	$Cs_2LiLaBr_6(Ce)$
FoM	Figure of Merit
SEE	Single Event Effect
ALPI	Acceleratore Lineare Per Ioni (in Italian)
LINAC	Linear Accelerator
SF	Spontaneous Fission
DAQ	Data Acquisition
MC	Monte Carlos simulation
FPGA	Field Programmable Gate Array
PSD	Pulse Shape Discrimination
DPP	Digital Pulse Processing
ADC	Analog-to-Digital Converter
SiPM	Silicon Photomultiplier
SPAD	Single Photon Avalanche Diode
RGB	Red, Green, and Blue light
INFN-LNL	National Institute of Nuclear Physics in Legnaro
PCB	Printed Circuit Boards

Chapter 1

Introduction

Due to the advancements in nuclear physics and its applications, the use of radioactive materials has witnessed a substantial growth over time. Nowadays, radioactivity is used in an ample amount of applications ranging from medical (diagnosis and treatment), archaeological (dating and tomography), commercial (sterilizing goods), and many more. Accordingly, the need to identify and quantify different isotopes as quickly and efficiently as possible can prove detrimental to the protection of human lives, particularly, in the cases of Special Nuclear Materials (SNM) or natural disasters. SNM are defined to be materials that are fissionable, highly radioactive, and cannot be found in nature; these isotopes are ^{235}U, ^{233}U and ^{239}Pu [1]. These materials are mainly present in nuclear reactors and military research facilities with nuclear propulsion vessels. They can be used to manufacture nuclear weapons and radiological dispersal devices (RDD) (known as Dirty Bombs) [2]. As the number of illicit trafficking of SNM and nuclear material that can pose a threat to nations' stability and civilians' lives has substantially increased over the past few years, developing redundant ways to deal with them has become a major need. As reported by the International Atomic Energy Association's (IAEA) Incident and Trafficking Database (ITDB), 3928 radiation related incidents have taken place between the period of 1993 and 2021, 320 out of them were classified as incidents likely connected to trafficking or malicious use. Furthermore, the rest of the incidents were related to lost, stolen, or improperly disposed sources most of which are long lived elements such as ^{137}Cs used for industry [3].

To solve this problem, many countries have deployed an ample amount of monitoring stations at their borders, airports, and seaports. These stations typically contain neutron and/or gamma detectors able to utilize different techniques such as Fast Neutron and Gamma Transmission (FNGT) to identify the elements without physical interaction that can endanger human lives [4]. Moreover, all power plants must contain detection systems to help control and maintain the reactor operating without any disasters. However, in the case of disasters such as the Fukushima Daiichi incident on March 2011 where a tsunami rendered all surveillance systems futile, a mobile detection system can prove vital for first responders [1]. Such mobile solutions can come in the form of a UGV (Unmanned Ground Vehicle) or UAV (Unmanned Aerial Vehicle) that can cover harsh terrain while carrying different detectors as close as possible to the radiation source which eliminates any risk to human lives.

The main objective for such measurements is to identify and/or quantify the type of radiation and its source (isotope) over a certain area. This aligns with the objectives of the DRAGoN (Drone for Radiation Detection of Gammas and Neutrons) project which aims to design, develop, and characterise a detection system to be placed on a UAV. It can detect SNM over an area thanks to its high gamma and neutron (fast and thermal) discrimination capabilities. The project is a collaboration between Padova and Terento Universities and financed by INFIN (Istituto Nazionale di Fisica Nucleare) [5] [6].

The detection system placed on the drone for the DRAGoN project is comprised of two interchangeable systems with the same readout for different situations. The first system is a radioactivity counter monitor using a plastic scintillator (EJ-276 70 mm diameter x 130 mm thickness) while the second is a radionuclide identification system using an inorganic scintillator (CLLB 50.8 mm diameter x 50.8

mm thickness). Both systems are connected to a CAEN digitizer and a control system [6].

In addition to identification of SNM, neutron detection is extremely useful especially for nuclear structure experiments performed using Radioactive Ion Beams (RIBs) as these neutrons can provide extra information and facilitate measurement techniques such as missing mass. One of the aims of the new SPES project currently under construction at INFN LNL (Laboratori Nazionali di Legnaro) is to provide RIB using ISOL technique to be used for nuclear physics experiments in the foreseen future [7].

The objective of this work is to characterize organic and inorganic scintillators to be used in the DRAGoN project as well as the upcoming neutron detection system for SPES experiments using different readout devices such as PMT and SiPM in order to study their performance and determine their light output function. In order to achieve such characterization, different radioactive sources will be used for the calibration in addition to proton and neutron beams with different energies to find the light output function. The organic scintillator used will be a plastic scintillator EJ-276G (25.4 mm diameter x 25.4 mm thick) [8] that will be coupled to a new SiPM model (S14161-6050HS-04) Hamamatsu SiPM array which is sensitive to the RGB range of wavelengths [9].

Subsequently, the scintillation detector will be assessed while being coupled to the novel scintillation detector ($^{6}Li_{2}^{10}B_{4}O_{7}$ or LiBO) developed in INFN to detect thermal neutrons [10]. All the tests will be run using two CAEN digitizers, a desktop DT5725 (250 MHz sampling frequency) and a VME V1730 (500 MHz sampling frequency) [11]. The entire setup will also be tested with the specifically designed circuit for the SiPM in order to ensure stability and compactness as both the payload of the drone and the experiment which was designed by the (engineering team) in INFN LNL lab.

The main goals of the characterization are to determine and optimize the discrimination capabilities of the detector between gamma photons and fast neutrons and find the optimal light output function. Following, the discrimination capabilities of the whole setup (EJ-276G + LiBO) between gammas and neutrons (fast and thermal) will be studied in order to determine the optimal combination of plastic and LiBO that provides satisfactory properties to the DRAGoN project as well as the possible experiments at SPES.

Chapter 2

Literature review

2.1 Scintillation detectors

Since their discovery in 1903, scintillation detectors have been under constant development which made them the preferred choice for a myriad of applications. They combine robustness, low maintenance, good energy and time resolution with a decent price. In principle, all scintillation detectors are comprised of a scintillation material where the energy of the photon is deposited and a photon of visible light or ultraviolet is produced via one of the processes to be discussed in the following sections. Subsequently, a photocathode converts the produced photon to an electron via photoelectric effect. Finally, some electron multiplication device multiplies the number of electrons to form a charge signal that can be picked up by a digitizer. Although the mechanism of scintillation may vary from one type of scintillation material to another, the ideal scintillation material should, in principle, poses the following properties [12] [13].

- Convert kinetic energy of charged particles (or energy of photons) into detectable photons with high efficiency and linear conversion such that the light produced is proportional to the energy deposited in the material.
- The decay time should be short to enable the generation of fast signal pulses.
- The medium must be transparent to the wavelengths of its own emission to prevent light loss by absorption.
- It should have adequate optical properties and a refraction index of (1.5) to facilitate its coupling to a photocathode device.

In reality, there is no scintillation material that exhibits all these properties simultaneously, however, the choice of the preferred qualities highly depends on the desired application. Generally, scintillation materials can be categorized into **Organic scintillators** and **Inorganic scintillators**.

In general, the prime difference between **organic** and **inorganic** scintillators is the atomic number **Z** of the material which dictates what type of interactions it will have with the impinging radiation, hence, the species to which it is most sensitive.

2.1.1 Organic Scintillators

Organic scintillators, typically, are mainly comprised of low Z-value elements such as (hydrogen, carbon, and oxygen) which makes them perfect for the detection of charged particles such as beta and alpha. However, due to their low Z-value, they practically have no cross section for *photoelectric* interaction for gamma rays of relevant energies as observed in Fig. 2.1. Consequently, they exhibit no photopeaks and solely operate in Compton edge regime [12] [13].

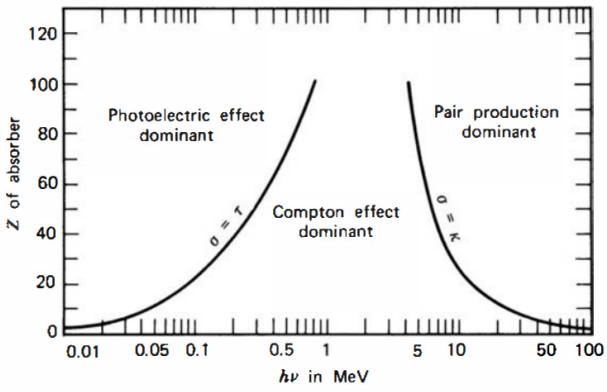

Figure 2.1: Different gamma interactions depending on energy and mass number. [12]

Organic scintillators can be mainly divided into 5 categories which are pure organic crystals, liquid organic solutions, plastic, thin film, and loaded organic scintillators. Liquid organic solutions are produced by dissolving an organic scintillator into a solvent and occasionally adding some material that acts as a wavelength shifter to accommodate the emission spectrum to the PMT wavelength sensitivity region. They can usually be made into large volumes and are characterized by a very high radiation hardness (can withstand a dose up to 10^5 Gy) due to their lack of crystalline structure. However, in the case where robustness is needed, plastic scintillators provide a great alternative. They are made by dissolving the organic scintillator in a material that can be polymerized such as a styrene monomer. Due to the ease at which the plastic can be fabricated and its relatively low price, it has become a preferred choice for many applications [12].

Scintillation mechanism in organic scintillators

The luminescence process taking place in organic scintillatros arises due to the transitions between energy levels of single molecules (when an electron is excited by the radiation and later de-excite to ground level), therefore, it is independent of the physical state of the material (solid, liquid, or gas), unlike inorganic scintillators where a crystalline structure is vital to the emission of scintillation light. Contrary to inorganic compounds, organic scintillators form by a molecular crystalline structure in which molecules are loosely bound by Van Der Waals forces [13]. The structure of organic molecules is mainly established by the electronic structure of the carbon atoms (Z=6) which have an electronic configuration at ground state of $1s^2\ 2s^2\ 2p^2$. However, when a C atom forms a compound, one of electrons in 2s is excited to the 2p leading to a ground state configuration of $1s^2\ 2s^1\ 2p^3$. These four states become mixed or "hybrid" and different configurations can be attained. Depending on the symmetry of of the orbitals, one could have σ-electrons forming σ-bonds or π-electrons forming π-bonds. While σ-orbitals can provide σ-bonds for C-H and C-C, the two π-orbitals interact forming a π-bond for C-C at maximum interaction. The π atomic orbitals of two carbon atoms interact forming a covalent bond with a common nodal plane where π electrons reside. These excited states of these π electrons gives rise to the luminescence of the molecules. The π electronic energy levels are demonstrated in Fig. 2.2 [12] [13].

Energy of the charged particles can be absorbed by any of the singlet (spin=0) states $S_0, S_1, S_2, \ldots$ up to the ionization energy I_π. For molecules of organic scintillators, ΔE between S_1 and S_0 is typically 3 or 4 eV while it is smaller for higher states. There are vibrational sub-levels dividing each electron configuration into many levels with much smaller ΔE often of the order of 0.15 eV. In order to distinguish these vibrational states, another subscript is added to the symbol of each state such that, for example, the lowest vibrational state of the ground state is S_{00}. Additionally, there exists a series of excited π electron triplet states denoted T_0, T_1, T_3, ..., that have lower energies than their corresponding S state. Furthermore, each of these states is also subdivided into vibrational sub-states and the transition from S_0 to T_1 is spin-forbidden [12] [13]. All molecules of the organic scintillators are

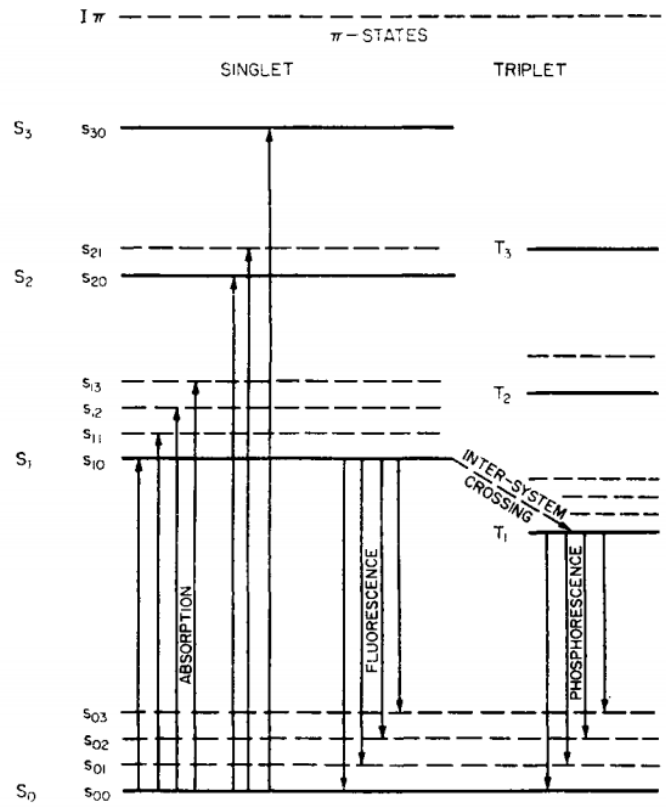

Figure 2.2: Energy levels of an organic molecule with π-electron structure [12].

in S_{00} state at room temperature as the spacing between vibrational states is substantial in comparison with thermal energies ~ 0.025 eV.
As demonstrated in Fig. 2.2, when a charged particle passes in the organic scintillator it can excite any of the singlet states by absorption of the energy. The de-excitation of these states eventually causes the luminescence which can be divided into three types:

- Fluorescence
- Phosphorescence
- Delayed fluorescence

Fluorescence represents the transition from S_1 to S_0 which customarily has a lifetime $\sim 10^{-8}$ to $\sim 10^{-9}$ seconds. This lifetime is much longer than the period of molecular vibration ($\sim 10^{-12}$ seconds) which allows the molecule to thermally equalize before emission. Although excitation of the pi electrons can take place to any singlet state, the fluorescence has the same characteristic emission spectrum, decay time, and quantum efficiency. This is due to the hastily ($\sim 10^{-11}$ sec) radiationless internal conversion that takes place lowering all higher excited states (eg. $S_1, S_2, \dots$) to S_1 which is subsequently lowered via a series of thermal degradation to S_{10} where the fluorescence takes place. Intensity of the fluorescence emission **I** decays exponentially following

$$I = I_0 e^{\frac{-t}{\tau}} \tag{2.1}$$

Where **t** is the time, $\mathbf{I_0}$ is the initial intensity (t=0), and τ is the fluorescence decay time for S_{10}. Some of the π electrons in S_1 can transition without radiation to the long-lived triplet state (T_1) via a process called "inter-system crossing". This state can later de-excite by **phosphorescence** or **delayed fluorescence**. The lifetime of T_1 is typically of the order of 10^{-4} sec up to seconds. If a de-excitation from T_1 to S_0 takes place, it is called *phosphorescence* which has a similar vibrational spectrum to

that of *fluorescence* since the transitions taking place can end up in multiple vibrational sub-states of S_0. However, if the molecules acquire sufficient thermal energy to return to S_1, this can cause what is called *delayed fluorescence* which has the exact spectrum as fluorescence but its decay period is of the order ($\sim 10^{-6}$ seconds) instead; delayed fluorescence does not have the same exponential behaviour as fluorescence [12] [13].

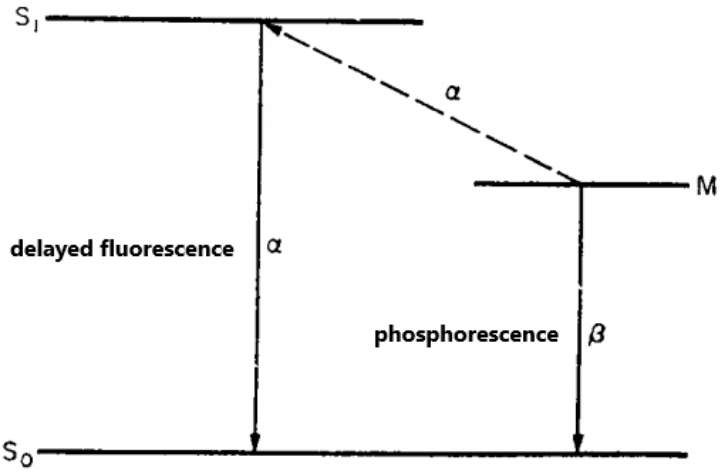

Figure 2.3: Proposed origin of delayed fluorescence (α-process) and phosphorescence (β-process) from meta-stable state M [13].

Furthermore, there exists a meta-stable state M between S_1 and S_0 typically populated by non-radiative conversion from S_1 as highlighted in Fig. 2.3 where two competing processes may take place that also cause phosphorescence and delayed fluorescence. Two competing processes may take place for the transition from M. If a slow transition occurs to the ground state S_0, it is called a β-process which causes phosphorescence. Alternatively, if enough thermal activation energy is acquired over time to excite back to S_1, it will de-excite as a delayed fluorescence which is called α-process. Both the phosphorescence and delayed fluorescence emissions cause what is called "afterglow" which is considered , in most cases, as a negative effect that should be minimized and accounted for as it causes the radiation intensity to change rapidly increasing the unwanted background [13].

Scintillation efficiency is defined as the fraction of all the energy deposited by charged particle into the material that is transformed into visible light. It is generally desired to have the highest efficiency possible. However, there is an ample amount channels for the de-excitation and most of them are not through scintillation but mainly heat. These radiationless de-excitations are called *quenching* and their sources must be minimized during the fabrication of the scintillator by, for example, eliminating impurities in the material such as oxygen in the solvent [12].

As mentioned before, most organic scintillator are fabricated from at least two components (some organic solvent and scintillation material), however, occasionally another material called "waveshifter" is added in order to absorb the scintillated light and re-emit it with a longer wavelength. This is usually done in order to accommodate the emitted light with the optimal wavelength range of the PMT or SiPM used [12].

Light response in organic scintillators

The proportion of the K.E of the charged particle utilized in the scintillation process is dependent on the impinging particle type and energy. For particle energies above 125 keV, the response to electrons is linear. However, the response for other charged particles such as protons and alpha particles is nonlinear for low energies and always less than that of the electron as can be illustrated in Fig. 2.4.

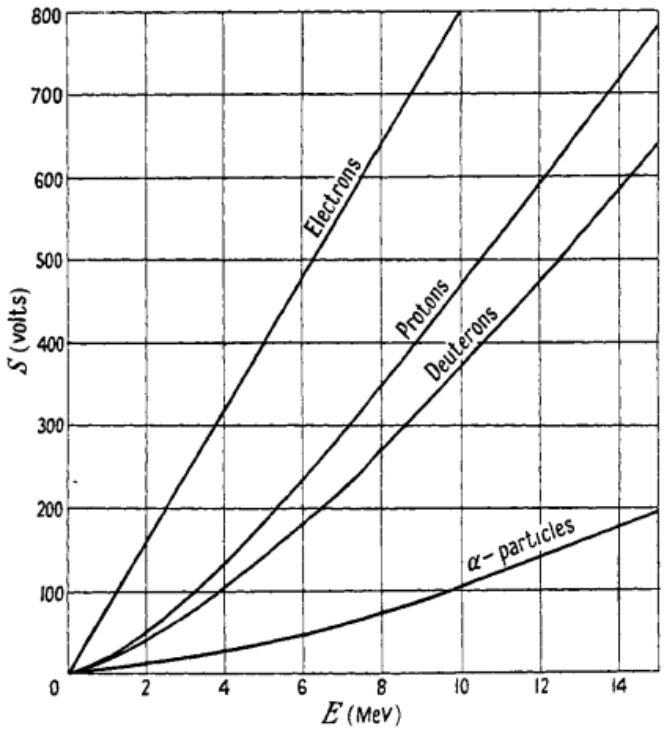

Figure 2.4: Relative scintillation response S of anthracene to particles of energy E [14].

Consequently, an absolute light yield was formulated in the form of *MeV electron equivalent* (MeVee) which is defined as the particle energy required to produce 1 MeVee. By definition, a fast electron will require 1 MeV to produce 1 MeVee. However, other particles will require much more energy to produce 1 MeVee [12]. In order to best explain the response of organic scintillators, Birks assumed that a substantial ionization density along the track of a charged particle will leads to a decrease in the scintillation efficiency due to a quenching caused by the damaged molecules [12] [15]. In the absence of quenching, the light response should be

$$\frac{\mathrm{dL}}{\mathrm{dx}} = \mathrm{S}\frac{\mathrm{dE}}{\mathrm{dx}} \tag{2.2}$$

Such that $\mathbf{\frac{dL}{dx}}$ is the fluorescent energy emitted per unit path length, $\mathbf{\frac{dE}{dx}}$ is the specific energy loss for the charged particle, and **S** is the normal scintillation efficiency.
When the scintillation material is excited by fast electrons (either directly or from gamma-ray irradiation), for large values of E $\frac{\mathrm{dE}}{\mathrm{dx}}$ is small. Then 2.2 becomes

$$\frac{\mathrm{dL}}{\mathrm{dx}}\Big|_{\mathrm{e}} = \mathrm{S}\frac{\mathrm{dE}}{\mathrm{dx}} \tag{2.3}$$

Then the light output per unit energy loss is

$$\frac{\mathrm{dL}}{\mathrm{dE}}\Big|_{\mathrm{e}} = \mathrm{S} \tag{2.4}$$

Then the light output **L** is

$$\mathrm{L} \equiv \int_0^{\mathrm{E}} \frac{\mathrm{dL}}{\mathrm{dE}}\,\mathrm{dE} = \mathrm{SE} \tag{2.5}$$

This verifies the linearity of the of the light output to the initial particle energy **E**. Assuming density of damaged molecules along the particle's is directly proportional to the ionization density, their

density can be described by $B(\frac{dE}{dx})$ such that **B** is the constant of proportionality [12] [15]. Under the assumption that only a fraction of these molecules will cause quenching, the *Birk's formula* can be written

$$\frac{dL}{dx} = \frac{S\frac{dE}{dx}}{1 + kB\frac{dE}{dx}} \tag{2.6}$$

Nevertheless, unlike electrons, the energy loss $\frac{dE}{dx}$ for alpha particles is substantial which generates saturation along the track of the charged particle and 2.6 becomes

$$\frac{dL}{dx}\Big|_{\alpha} = \frac{S}{kB}, \tag{2.7}$$

Then the kB value can be computed as follows

$$kB = \frac{\frac{dL}{dE}\Big|_{e}}{\frac{dL}{dx}\Big|_{\alpha}} \tag{2.8}$$

Pulse Shape discrimination (PSD)

For organic scintillators the majority of the observed scintillations arise from the prompt fluorescence. However, there is a probability for a delayed fluorescence which has similar exponential behaviour as that of the prompt one with a life-time of several hundreds of nanosecond. The profile of this delayed fluorescence depend on the type of the exciting particle, hence, it can be used discriminate between different species of particles by observing the tail of the of the light intensity (since it depends on the sum of prompt and delayed fluorescence). This technique is called *Pulse Shape Discrimination* (PSD) [12].

This delayed fluorescence mainly arises from the excitation of a triplet state (T_1) when the electron gains thermal energy and re-excites to S_1 where it can de-excite to the ground state giving rise to the delayed fluorescence. The inconstancy in the yield of the slow component can be attributed to the different densities of the various triplet states excited along the path of the charged particle. Hence, the slow component fraction of the light yield should depend mainly on the rate of energy loss $\frac{dE}{dx}$ of the exciting particle which explains the longer tail of heavier particles as they have much higher energy loss inside the scintillator as shown in Fig. 2.5 [12].

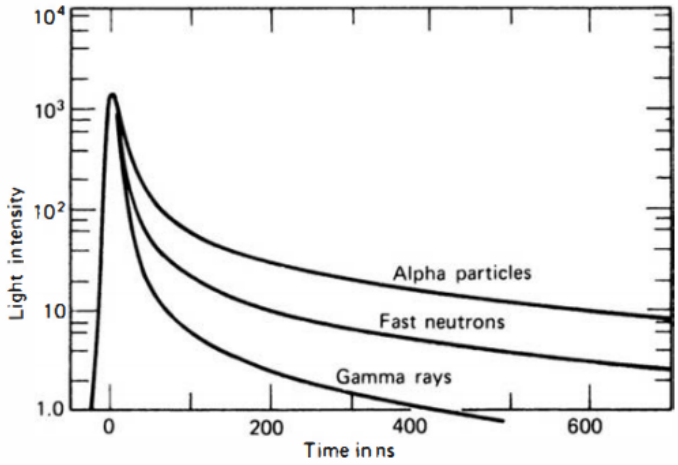

Figure 2.5: The time dependence of scintillation pulses in stilbene (equal intensity at time zero) when excited by radiations of different types [12].

2.1.2 Inorganic scintillators

Unlike organic scintillators, inorganic scintillators are usually comprised of compounds with high Z-value such as NaI and CsI which allows them, in addition to Compton interactions, to have *photo-electric* interactions with photons at relevant energies. This fact makes them perfect for spectrometry applications as the full energy of the photons emitted by radioactive nuclei can be absorbed by the crystal and the energy of the photons can be computed.

Scinitllation mechanism in inorganic scintillators

The mechanism of scintillation inside an organic scintillator can be understood using the band theory of crystalline lattice in solids. In a pure crystal, the energy states of an isolated atom or molecule consist of discrete levels. However, the outer levels may be perturbed by mutual interactions between the atoms or ions which causes these discrete levels to split into a sequence of "allowed" energy bands separated by regions where the electrons can never exist known as "forbidden bands" as highlighted in Fig. 2.6.

An energy gap E_g of a few electron-volts separates the highest filled band known as "valence band" where electrons are typically bound at the lattice site from the lowest empty band known as "conduction band" where electrons that have gained enough energy to be able to move around the crystal freely reside. If an electron from the valence band gains enough energy from a photon to overcome the energy gap E_g, it can move to the conduction band leaving a hole which would enable photo-conduction to take place. Nevertheless, in insulator crystals this process in highly inept, moreover, upon de-excitation of the electron from the conduction band to the valence band, the photon emitted will have a wavelength much higher than that of visible light [12] [13].

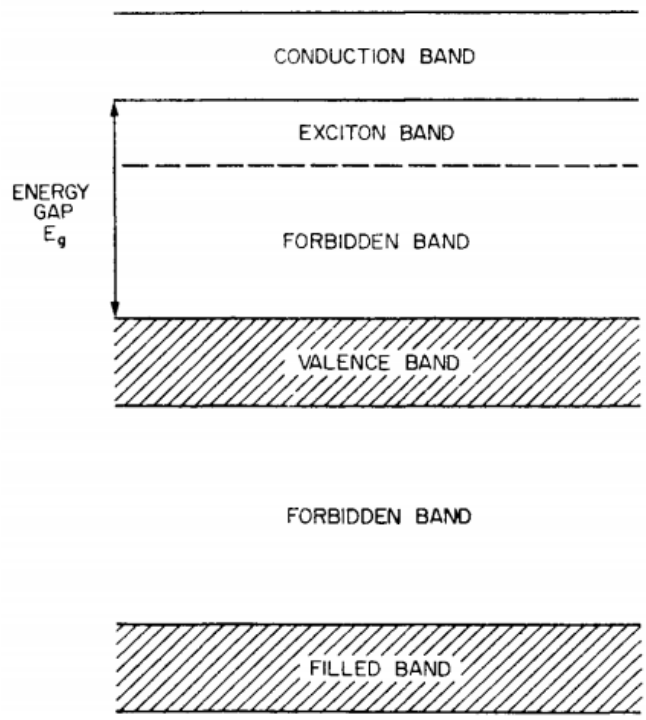

Figure 2.6: Energy bands in ideal insulating crystal [13].

In order to solve such problem and improve the probability of a visible photon being emitted, a small fraction (typically 1 part per thousand) of an impurity is added that is called "activator". The primary function of this activator is to modify the band structure by adding extra levels in the forbidden band near the valence band (activator ground state) and near the conduction band (activator excited state) as demonstrated in Fig. 2.7 [12].

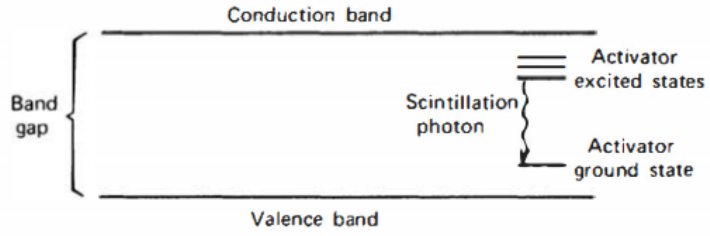

Figure 2.7: Energy band structure of an activated crystalline scintillator [12].

As a charged particle passes through the scintillation material, it will excite multiple electrons from the valence band to the conduction band creating holes in the valence band as a result. Due to the existence of the activator ground state which is close in energy to the valence band, electrons can undergo radiationless de-excitation filling the holes in the valence band which creates holes in the activator ground state. Similarly, electrons in the conduction band can de-excite without radiation to one of the activator excited states as their energies are close to that of the conduction band. The transition of the electrons from the activator excited states to its ground state emits a photon that can be in the visible light range upon the proper selection of the activator material. Alternatively, an electron can have an excited configuration at the activator center that has a forbidden transition to the ground state which leads to a delay of the de-excitation until sufficient energy is gained to enable an allowed transition to the ground state. This leads to a *phosphorescence* light known as "afterglow" which is considered as a source of background [12] [13].

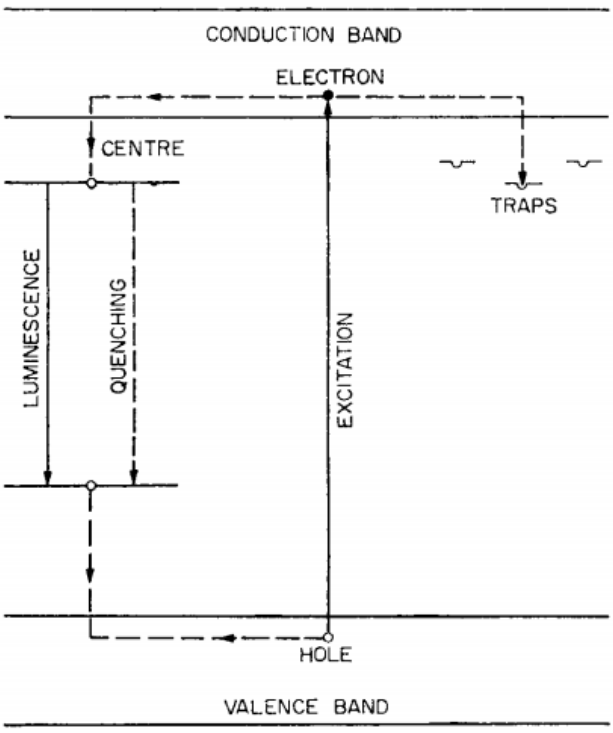

Figure 2.8: Energy bands in impurity-activated crystal phosphor, showing excitation, luminescence, quenching and trapping processes [13].

It should be noted that the activator centers created in the lattice following the doping process can have three types (Fig. 2.8):

- **Luminescence** centers where the transition to the ground state is accompanied by the emission of a photon.
- **Quenching** centers where thermal dissipation of the excitation energy takes place without the emission of radiation.
- **Traps** that have metastable levels where the electron can obtain thermal energy from the vibrations in the lattice and be excited back to the conduction band (or de-excited back to the valence band) without emitting radiation.

One center may contain one or more of these types where the relative population of each level depends on Boltzmann's distribution [13].

2.2 Neutron detection in scintillation detectors

The detection of neutrons is considered a cumbersome process as neutrons have no charge and can travel several centimeters inside a detection material before losing all its energy. Neutrons can be characterized depending on their energy into many categories, however, for the sake of this discussion, the categorization can be limited to neutrons with high energy (above 1 MeV) which are called *"fast neutrons"* and and ones with low energy (0.025 eV) which are known as *"thermal neutrons"*. Generally, neutrons can have two types of interactions with differing cross sections depending on their energy and the type of target nucleus.

2.2.1 Scattering interaction

These interactions are the prime interactions for the detection of **fast neutrons** as their high energy makes the reaction with dominant cross section be the scattering with a proton (Hydrogen) $^{1}\mathrm{H(n,n)}^{1}\mathrm{H}$ as highlighted by Fig. 2.9. The primary interaction in this case is the elastic scattering of protons by the neutrons (n,p) process [13].

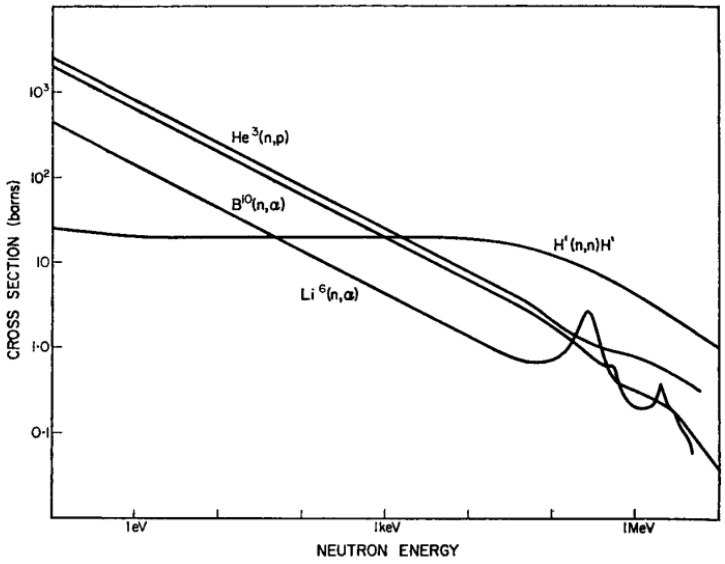

Figure 2.9: Log-log plot of neutron absorption or scattering cross-section against neutron energy for the four main neutron detection processes [13].

Following equation 2.9, it can be noted that when the mass number of the target **A** is equal to 1 (for a proton), the maximum transferred energy (for head-on collision) $\mathbf{E_{max}}$ equals the energy of the neutron $\mathbf{E_n}$ which indicates (approximately) a full energy transfer [13].

$$\mathrm{E_{max}} = \frac{4\mathrm{A}}{(\mathrm{A}+1)^2}\mathrm{E_n} \tag{2.9}$$

2.2.2 Absorption interactions

These interaction are dominant at lower energy of the neutron, in particular, at thermal energies ($\sim$ 0.025 eV) where neutron capture has higher cross section. Depending on the mass of the target nucleus, there could be three different reactions (n,γ), (n,α), (n, p), or (n, fission). Interactions with light nuclei mainly involve the emission of a charged particle which can then be detect by the scintillation material. Fig. 2.9 highlights different cross sections of neutron interactions with different elements at different energies [12] [13].

2.3 Photomultipliers

In order to convert the light emitted by a scintillation material into some electric signal that can be processed, a *photodetector* must be deployed. A photomultipler serves two distinct purposes which are the conversion of light to electrons and the multiplying of these electrons. The light produced by scintillation is typically feeble. Accordingly, photomultiplers need a large internal gain to be able to convert these few photons into a detectable signal.

2.3.1 Photomultipler Tube (PMT)

A photomultiplier tube (shown in Fig. 2.10) is a vacuum tube that contains a glass window, photocathode, and a number of metal dynodes.

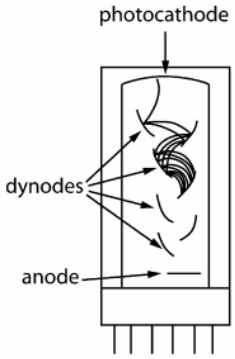

Figure 2.10: Schematic representation of a photomultiplier tube and its electrode geometry [16].

The photocathode is a thin layer of a material that can utilize photoelectric effect to absorb photons of visible (or near visible) light and convert them into electrons. The main features to consider for the photocathode are its thickness (needs to be greater than the maximum escape depth and to be supported by a thick backing material [12]), and its quantum efficiency (must be as high as possible). Not all the electrons impinging on the photocathode will be converted into electrons, accordingly, a unit for scintillation counting must be introduced which is the *quantum efficiency* (QE) that can be defined as

$$\text{QE} = \frac{\text{Number of photoelectrons produced}}{\text{Number of incident photons}} \tag{2.10}$$

An ideal photocathode should have 100% QE, however, most common PMTs have 20-30% only [12].

The photocathode is kept at a voltage that is negative with respect to the dynodes (typically of the order of kV). Following its production at the photocathode, the electron is accelerated towards the anode due to the potential difference. Upon hitting the first dynode, the electron's kinetic energy is sufficient enough to extract several electrons from this dynode. These electrons in turn are accelerated to the next dynode where the process repeats and the electrons are multiplied. By the time the electrons reach the final dynode, their number would have multiplied by a factor of 10^6 or more. These electrons are collected by the anode as the current to be processed [12] [16].

2.3.2 Solid-state photomultiplers

Although PMTs are most commonly used due to all their merits, they have several drawbacks depending on the application such as their high price, fragility, high power consumption, and sensitivity to magnetic fields. These drawbacks coupled with the great advancements in the photodiode technology over the years have led to a wide spread of the use of diode photomultipliers as a replacement to PMT for some applications. solid-state photomultiplier has multiple pros such as its superior quantum efficiency (due to the absence of the need for the electrons to punch through the photocathod) that can reach up to 80% at peak QE which can lead to a better energy resolution, it uses exponentially less power than a standard PMT, external magnetic fields essentially have no effect on it, it is compact and durable, and good time response can be achieved using it due to the small distance the charges need to travel in the device.

Avalanche photodiode (APD)

Unlike conventional photodiodes that have no internal gain and at best can produce number of electrons equal to that of the number of photons impinging on them as shown in Fig. 2.11, an APD has a different structure and can provide an internal gain that allows the possibility of its use without further amplification.

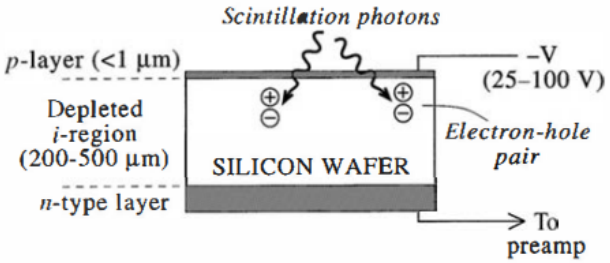

Figure 2.11: Basic configuration of a conventional photodiode (PIN) [12].

An APD can have several methods of fabrication, however, the most common one is the *reach-through configuration* in which the APD is comprised of a heavily doped region **p+** followed by a large intrinsic region π then a lightly doped region **p** followed by a heavily doped region **n+** where the bias applied in reverse as shown in Fig. 2.12 (where **p** means excess holes, **n** excess electrons and the + denotes heavy doping) [12]. When light impinges on the ADP through the anode (p+), some electron-hole pairs are generated in the π region. Due to the high electric field provided by the bias, the electrons travel through the drift region to the multiplying region with the highest electric field. Upon reaching the multiplication region (p-region), the high K.E. of the electrons causes an avalanche (process called impact ionisation) analogous to that produced in Geiger-Muller counter; this avalanche provides a gain factor of a few hundreds. The electrons are then collected at the cathode to provide the electrical signal as shown in Fig. 2.12. When this current is quenched by the series of resistors after the cathode, the reverse voltage is decreased and the diode returns back to its original bias voltage; it is then ready to detect another photon [17].

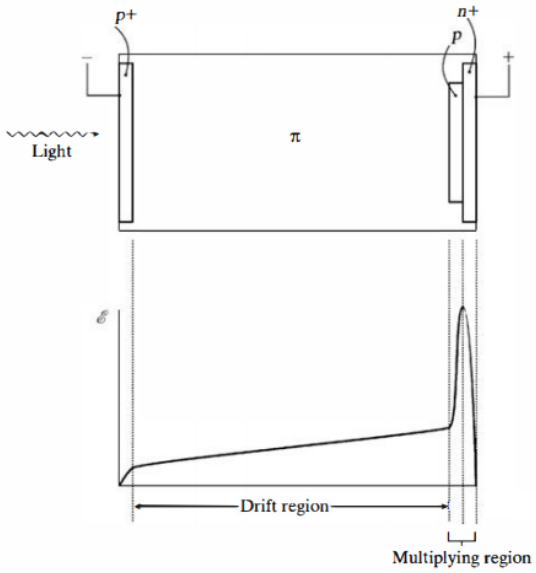

Figure 2.12: The reach-through configuration for an avalanche photodiode is sketched at the top of the figure. Below is a plot of the resulting electric field when a bias voltage is applied [12].

The internal gain gain cause by this process is high enough to enable good energy resolution for low energy radiation, however, the gain is highly affected by temperature variance (reduction of 2% for every 1°C) which is inadequate when using it for an outdoor condition. To solve this problem, the APD is conventionally connected to a circuit using a stabilization scheme to adjust the bias voltage based on the current temperature of the diode [12].

Silicon photomultiplier (SiPM)

As previously mentioned, upon being hit by a photon, the APD becomes idle until its bias voltage stabilizes. In this time, it will not be sensitive to any other photons that impinges on it. To solve this conundrum, SiPM is used. It is comprised of a matrix of single photon avalanche diodes (SPAD) connected in parallel as shown in Fig. 2.13. Each of them is connected in series with a quenching resistor R_q and operating in Geiger-mode (GM) with a reverse bias voltage V_{bias} beyond the breakdown voltage V_{br} (voltage beyond which the diode can maintain the avalanche process) such that V_{bias} is

$$V_{bias} = V_{br} + V_{ov} \tag{2.11}$$

With V_{ov} being the excess voltage beyond V_{br}. Fig. 2.13 highlights the equivalent circuit of the individual microcells with R_s is the silicon substrate series resistance, C_d is the diode capacitance in reverse bias, R_q is the quenching resistor [18].

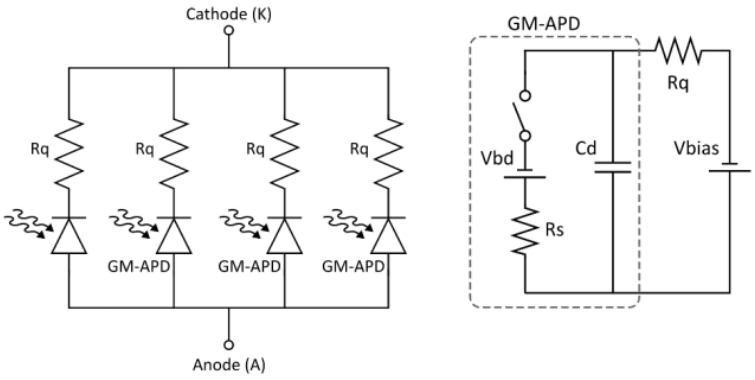

Figure 2.13: Left: Parallel arrangement of GM-APDs (SPADs) in SiPM. Right: Equivalent circuit of GM-APD and external bias with turn-on for the photon absorption and turn-off for the quenching [18].

There are three main phases for the operation of the microcells which are

- **Breakdown**: As the bias voltage is set to have a value greater than that of V_{br}, when a photon penetrates the diode, the switch in Fig. 2.13 is closed and the avalanche process takes place.
- **Quenching**: With the help of R_q, the voltage drops as the avalanche is quenched and the switch in Fig. 2.13 is open again.
- **Reset**: C_d recharges back to V_{bias} and the diode is operational once more.

Fig. 2.14 highlights the process above.

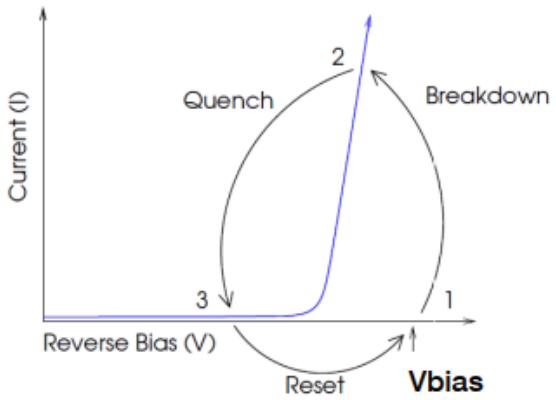

Figure 2.14: Cycle of operation of individual microcells. [17].

Gain of the SiPM is considered the total charge from all the microcells, accordingly it will depend on the gain of each individual microcell defined as

$$G_{APD} = \frac{V_{ov} \times C_d}{q} \tag{2.12}$$

With **q** being the electron charge. Hence, the total charge is

$$Q = N_{fired} \times G \times q \tag{2.13}$$

Such that $\mathbf{N_{fired}}$ is the number of fired microcells, and**G** is the gain on individual cells. This leads to the proportionality with the scintillation as the accumulated charge from all microcells should, in principle, be related to the number of photons produced by the scintillation material [18].

A typical SiPM contains several thousands of microcells per mm^2 [17], the recharge time (recovery time) of which is dependent on that of the microcell recharge time constant. This recharge time is defined as

$$\tau_{RC} = C_d(R_q + R_s \times N) \tag{2.14}$$

Where $\mathbf{C_d}$ is the effective capacitance of the microcell, $\mathbf{R_q}$ is the value of the quench resistor, **N** is the number of microcells in the SiPM, and $\mathbf{R_s}$ is any resistance in series with the SiPM. It can be noted from 2.14 that the recharge time is directly proportional to the capacitance of the microcell, hence, as the area of the microcell increases, so will the recharge time (ex. a 100 μm microcell will have a much greater τ_{RC} than that of a 20 μm one) [17].

Noise is a major cause of concern for SiPM. There are 3 main types of noise

- **Dark count**: There is a small probability for an electron-hole pair to be formed not from an impinging photon, but from thermal agitation. When this happens, the avalanche will take place and a pulse will be generated in that diode. This is called a *dark event*. This is why temperature is an important factor for SiPM [18].
- **Afterpulsing**: Carriers trapped in silicon defects during the avalanche can be released afterwards during the reset phase causing another pulse at the tail of the original one as shown in Fig. 2.15 [18].
- **Optical cross-talk**: During the avalanche process, some photons can be produced and reach the active region of a neighboring diode (or even in different area of the same diode) triggering an avalanche in it. This results in a greater peak (due to more than one cell firing simultaneously) or a delayed peak (due to the photon first diffusing then firing another cell.) This can be demonstrated in Fig. 2.15 [18].

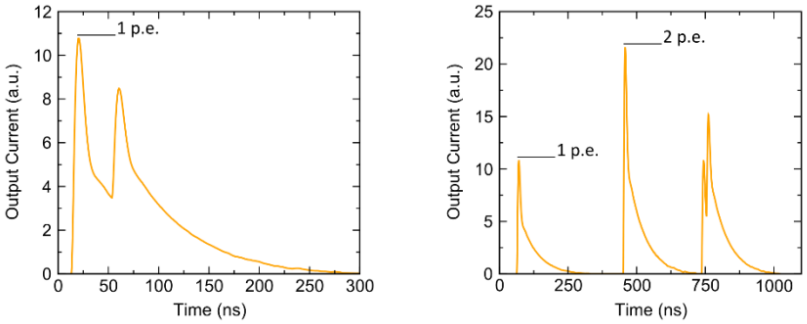

Figure 2.15: Left: Afterpulsing in SiPM for the same microcell (amplitude of second pulse is smaller than the first). Right:Optical cross-talk in SiPM. (Left to right:single cell firing, direct cross-talk, delayed cross-talk) [18].

2.3.3 PSD based on SiPM

Pulse shape discrimination technique is quite challenging with SiPM as it relies completely on the time profile of the light yield from the scinitllation process. The number of photons generated inside an organic scintillator by a 1 MeV electron, on average, are $\sim$ 10000 photons. Due to the GM behaviour of the SPADs constituting the SiPM, this means that if more than one photon impinges on the same microcell, only one will be detected. To provide solution for this conundrum, an ample amount of microcells are connected in parallel. It is crucial that the number of microcells in the SiPM be greater than the number of photons generated by the scintillator to allow the detection of the majority of scintillation photons. Another parameter to be considered is the recovery time of each microcell. The typical recovery time of each cell is between 10 to 100 ns which is generally in range of that of the fluorescence of the scintillator. Moreover, the area of the SiPM plays a major role in the efficiency of the PSD as covering the whole scintillator will maximize the number of scintillation photons detected. Generally, improving the PSD performance relies on the improvement of the *number*, and *recovery time* of the microcells as well as the size of the SiPM [19].

It is reported in [19] a comparison between the average pulses coming from an organic scintillator (EJ-299 20 mm diameter x 20 mm thickness) using a fast PMT and a SiPM matrix. It is obvious from Fig. 2.16 that the signal decay time of the PMT is superior to that of the SiPM, however, the discrimination between the neutron and gamma signals is still distinguishable.

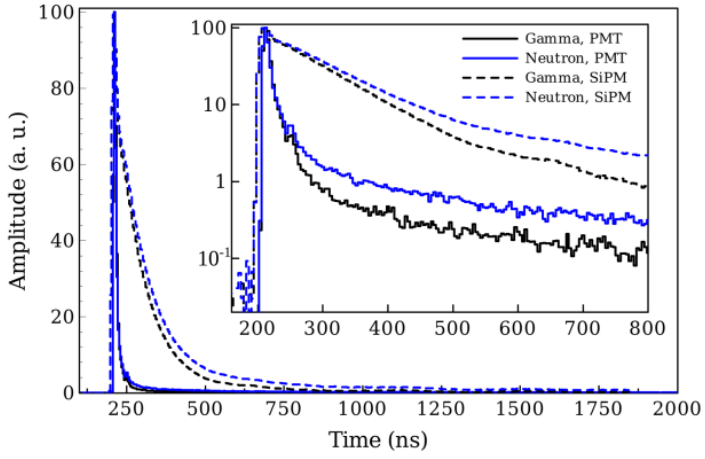

Figure 2.16: Neutron and gamma-ray average signals coming from the PMT anode and preamplifier output using EJ-299 (20 mm diameter $\times$ 20 mm thickness) [19].

2.4 Figure of Merit

Generally, there are two approaches to pulse shape discrimination. The first depends on the knowing the time differences in the rise time of the output pulse while the second is based on integrating the total charge over two distinct time periods. In this work, the second method has been utilized. It is based on the integrating the total charge over two different time regions of the pulse. Pulses with similar shape will have the same ratio between these signals regardless of the signal amplitude [12].

A parameter that can be used for the above method is the *Figure of Merit* (FoM) which is a measure of the ability of the system (detector and electronics) to differentiate between distinct types of event (ex. photons and neutrons). The results are expressed in a histogram called PSD plot where each peak would represent a particle species as highlighted in Fig. 2.17. The better the dissemination, the better the distinction between the two peak [12].

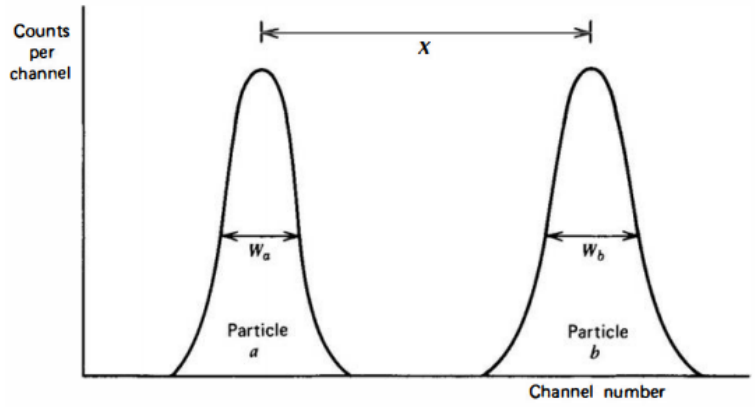

Figure 2.17: Definition of the figure of merit FoM for pulse shape discrimination applications. In the most common analog PSD method, the abscissa corresponds to the crossover time of a doubly differentiated input pulse [12].

The FoM value can be computed using equation 2.15 where $\mathbf{X_a}$, and $\mathbf{X_b}$ are the centroids of the two different particles (gamma photons and neutrons) and $\mathbf{W_a}$, and $\mathbf{W_b}$ are their Full Width Half Maximum (FWHM) values. The greater the FoM value the better the discrimination of the system as it means that $\mathbf{X}$ is greater (the peaks are well separated). Overall, a good FoM should be greater than unity. Furthermore, a full discrimination is attained at FoM > 1.27. This is because it means that $X > 3\sigma$ (FoM $= \frac{3\sigma}{2.35\sigma} = 1.27$) [12] [20].

$$\mathrm{FoM} = \frac{\mathrm{X}}{\mathrm{W_a} + \mathrm{W_b}} = \frac{\mathrm{X_b} - \mathrm{X_a}}{\mathrm{W_a} + \mathrm{W_b}} \tag{2.15}$$

2.5 Calibration of Organic scintillators

As mentioned above, organic scintillators depend on Compton interaction as their primary source of interaction with impinging photons due to their low atomic number Z. This interaction creates a pair of scattered photon and a recoiled electron with energy distributed amongst them depending on the scattering angle [12]. Considering that the energy of the impinging photon $\mathrm{E_\gamma} = \mathrm{h\nu}$, then the energy of the scattered photon will be

$$\mathrm{E_\gamma}' = \frac{\mathrm{E_\gamma}}{1 + (\mathrm{E_\gamma}/\mathrm{m_o c^2})(1 - \cos\vartheta)} \tag{2.16}$$

With $\mathbf{m_o c^2}$ being the rest mass of the electron (≈ 0.511 MeV), and ϑ is the scattering angle. From 2.16, the energy of the recoiled electron is

$$E_{e^-} = E_\gamma - E_\gamma{}' = E_\gamma \left(\frac{(E_\gamma / m_o c^2)(1 - \cos\vartheta)}{1 + (E_\gamma / m_o c^2)(1 - \cos\vartheta)} \right) \tag{2.17}$$

Two limiting cases take place in this case:

- When $\vartheta \cong 0$ (grazing angle scattering) in this case the photon retains almost all of its energy and the electron obtains no energy.
- When $\vartheta \cong \pi$ (head-on collision) in which the maximum energy transfer to the electron takes place with the electron moving in the direction of the initial photon. In this case, 2.16 and 2.17 become

$$E_\gamma{}' \Big|_{\vartheta=\pi} = \frac{E_\gamma}{1 + 2(E_\gamma / m_o c^2)} \tag{2.18}$$

and

$$E_{e^-} \Big|_{\vartheta=\pi} = E_\gamma \left(\frac{2(E_\gamma / m_o c^2)}{1 + 2(E_\gamma / m_o c^2)} \right) \tag{2.19}$$

The equations above are an approximation assuming that the recoil electron is initially free (or unbound) which is not the case. However, the binding energy is typically negligible with respect to the energy of the photon. All scattering angles ($0 \rightarrow \pi$) usually take place giving rise to the *Compton continuum* which ends with the *Compton edge* with max energy transfer as shown in Fig. 2.18. The gap between the Compton edge and the energy of the incident photon $\mathbf{E_C}$ (due to energy lost by scattered photon) is typically $E_C \cong \frac{m_o c^2}{2} = 0.256$MeV for large photon energy ($E_\gamma \gg m_o c^2/2$) [12].

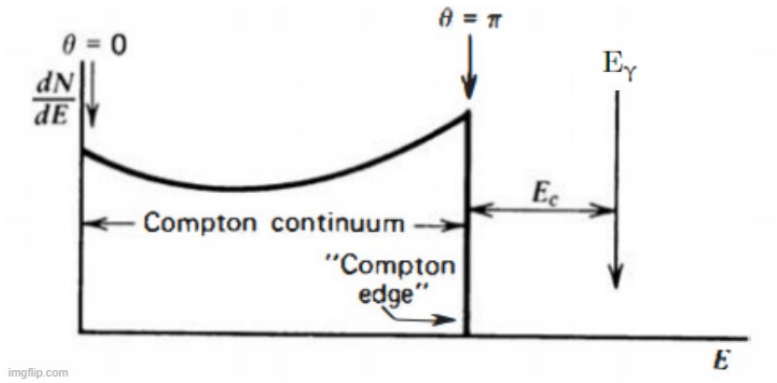

Figure 2.18: Electron energy distribution general shape for any one specific gamma-ray energy [12].

Chapter 3

DRAGoN Project and the Active Target for SPES

3.1 DRAGon Project

The **D**rone for **RA**diation detection of **G**amma and Neutr**oN**s (DRAGoN) project is a collaboration with the aim of designing, developing, and characterizing a mobile system of Unmanned Aerial Vehicle (UAV) equipped with detection system for gamma photons and neutrons, capable of identifying radioactive contamination spread across a specific area (of the order of tens of meters) [5]. The primary design requirements enable the detection of gamma-rays as well as fast and thermal neutrons in a high gamma-radiation background. These requirements are essential as the done will be used to detect SNM that can be easily shielded and difficult to detect with the natural background. Additionally, it will be deployed in cases of emergency where static detection systems fail to work or cannot be delivered such as in the case in Fukushima Daiichi or Chernobyl power plants.

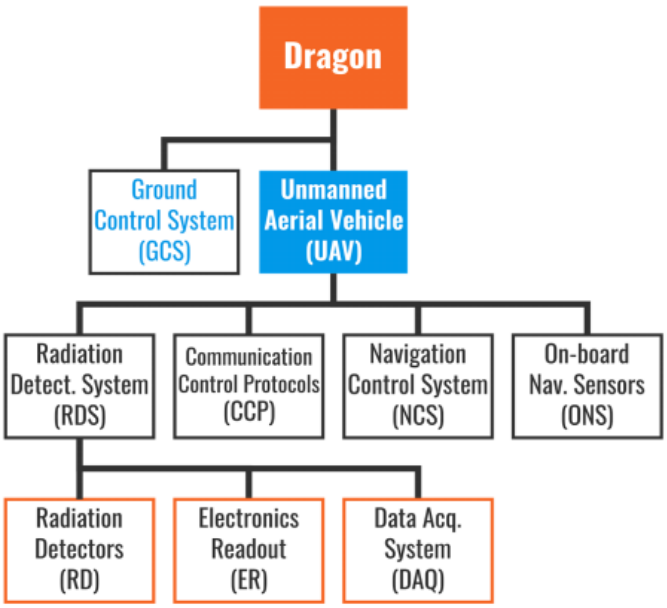

Figure 3.1: The DRAGoN project constituents scheme [5].

As highlighted in Fig. 3.1, the DRAGoN project consists of a UAV with all the vital subsystems to perform the measurements and control the flight, in addition to a Ground Control System (GCS) to control the UAV and receive online data. The GCS enables full control of the UAV via wifi have autonomous or real-time determination of the flight path [5].

3.1.1 Unmanned Aerial Vehicle (UAV)

There were multiple possible types of UAV considered including fixed wing or single helicopter style. However, a hexa-copter design (shown in Fig. 3.2) was found to be the most suitable as it provided the highest versatility in terms of position accuracy and stability [5].

The UAV is comprised of six propellers with brush-less motors designed to provide stability independent of the wind conditions. The Payload of the copter can be explained as

Figure 3.2: Tests with the assembled UAV. [5].

- *Navigation control system* (NCS) comprised of Pixhawk flight controller with a quadcore processor-based board which manages the flying parameters and connects the drone with the GCS.
- *On-board Navigation Sensors* (ONS) that provide vital flight information needed for the operation and stability of the drone.
- *Radiation Detection System* (RDS) that provides detection, processing, and data transfer.

3.1.2 Radiation Detection System (RDS)

The RDS of the drone is the most crucial part of the whole payload. Several conditions must be met by the RDS in order to perform its task such as high efficiency, low power consumption, minimal weight, and affordable price. It can be divided into three main categories as shown in Fig. 3.1 [5].

Radiation Detectors (RD)

In order to achieve the goals mentioned above, two solutions are considered for the RDS

- **Radioactivity counter** for which a plastic scintillator **EJ-276** is used due to its hardness and optical characteristics.
- **Radionuclide identification system** for which an CLLB is used due to its good resolution and radiation hardness against high dose (which makes it perfect for catastrophic events) [6].

A PMT is used for both solutions, however, to reduce the payload wight and power consumption, a large array of SiPMs has been incorporated instead of the PMT.

Electronic Readout (ER)

The detectors are coupled with a 125 MHz digitizer that allows real-time wireless measurements with an increased number of bits to compensate for the reduced sampling rate (to reduce the power consumption).

Data Acquisition System (DAQ)

The digitizer is controlled by a Field Programmable Gate Array (FPGA) that allows swift and efficient signal processing with a total processing time less than 10μs; this allows the collection of about 10^3 events/second. The DAQ has an embedded Linux operating system that allows data acquisition (DAQ) software to be installed such as ABCD which provides total control over the whole system [21].

3.2 Active Target for SPES

3.2.1 SPES Project

The **S**elective **P**roduction of **E**xotic **S**pecies (SPES) is considered the next step towards the new generation of European Ion Separation On-Line (ISOL) facility (EURISOL) that aims to provide high intensity neutron-rich beams to be used for a plethora of applications of fields such as biology, medicine, and material science (Fig. 3.3). The project is composed of four phases, SPES-α which aims for the installation of a proton cyclotron, SPES-β which handles the production and post acceleration of RIBs, SPES-γ which aims to produce radionuclides for medical applications, and SPES-δ which handles the production of neutron fields to be used for applied science studies such as material science (study of SEE) [19].

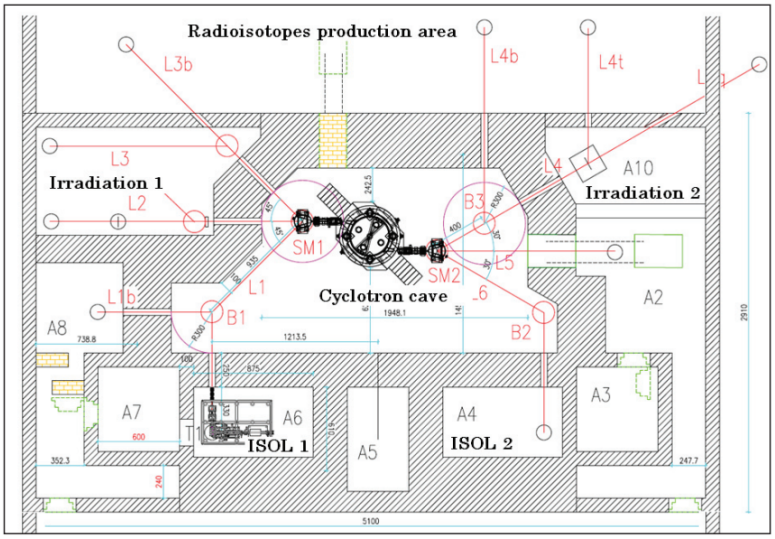

Figure 3.3: Partial layout of SPES proton beam distribution [7].

The ISOL facility operates via several steps that begin with a cyclotron accelerator that can provide a primary proton beam split into two ports with energies ranging from 30 to 70 MeV and a maximum beam current intensity of 0.750 mA for both of them combined. [7]. One of the proton beams with energy ∼70 MeV and intensity ∼ 500μA where it bombards a Lead target to produce neutrons for material research. While for the ISOL facility, the other proton beam with energy ∼40 MeV and intensity ∼ 200μA bombards a target of Uranium Carbide to produce a fission rate of ∼ 10^{13} fissions/second. This beam is later accelerated using an ALPI superconducting LINAC to produce a secondary beam with energy ∼10 AMeV (A = 80 – 130 amu) with intensity ∼ 10^8 pps [7].

3.2.2 Active target

In accordance with the goals of SPES-β, the development of an active target such as that of AcTar TPC is foreseen. This can be admitted to the fact that the experiments are done in reverse kinematics and the use of a thick target can reduce the quality of the experiment. Generally, an active target works by having a gaseous detector with an active medium consisting of a gas that is the target for

the reaction as well. An example to such detector is the Time Projection Chamber (TPC) used at Grand Accélérateur National d'Ions Lourds (GANIL) laboratory in France that can be illustrated in Fig. 3.4 [22].

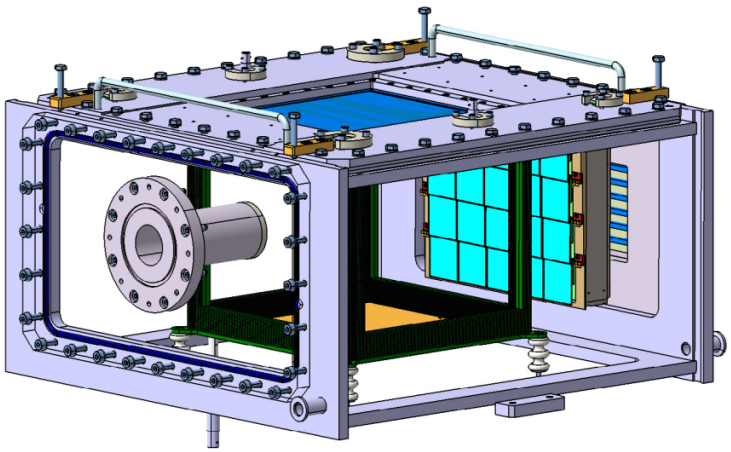

Figure 3.4: 3D computer-aided drafting (CAD) drawing of ACTAR TPC. [22].

It can provide 3D reconstruction of the tracks of the charged particles. However, such detectors usually require auxiliary detectors in order to boost their percussion and optimize their data acquisition capabilities. One of the considered auxiliary systems for the AcTar to be built for SPES is a system with neutron-gamma discrimination capabilities. This system must fulfil certain requirements such as compactness, robustness, and decent discrimination between gammas and neutrons [22].

3.3 Currently used Organic and Inorganic scintillators

3.3.1 UAV detection system

The concept of attaching radiation detectors to unmanned vehicles for different types of measurements has been around for years. Consequently, different types of scintillation detectors with varying designs have been considered for such occasion. For example, the work of [23] suggests using the scintillation material as a part of the body of the drone itself instead of being a payload to reduce weight of the drone. For this application, not only the light response and efficiency were the deciding factors, but also the mechanical properties as well. The author compared EJ-276 (which is very close in properties to EJ-276G used in this work) to multiple scintillators including EJ-200 which according to the author had improved mechanical properties than that of the EJ-276.

3.3.2 Secondary detection systems in nuclear physics experiments

In many nuclear physics experiments whether it is an active target experiment like AcTar TPC or experiments with liquid target like ones done at RIKEN, an auxiliary detection system for gammas and neutrons can greatly improve the quality of the data obtain and enable multiple levels of filtration. In this scenario, scintillation detectors can often prove to be an excellent candidate for this task as they can provide a balance between active area, efficiency, and price. In this case, the typical choice for good energy resolution is NaI(Tl) detector for its good price and adequate performance [24]. This is a prime reason why scintillation detectors like SrI : Eu or $LaBr_3$ are not considered as the best choice for such application even though they have substantially better resolution.

Chapter 4

Description of the experimental setup

In order to achieve the goals mentioned in the first chapter, the instrumentation, radioactive sources, electronic units, and software described in this chapter were utilized to characterize both the organic and inorganic scintillation detectors.

4.1 Scintillators

4.1.1 EJ-276G (Plastic Scintillator)

A plastic scintillator EJ-276G, produced by *Eljen Technology* (Based in Sweetwater, Texas, USA) was used in this work. This scintillator is characterized by its hardness and the ability to discriminate between fast neutrons and gamma-rays by utilizing the difference in the shapes of their respective signals due to the different decay times (PSD) [8].

The EJ-276G utilized was a cylindrical 25 mm diameter x 25 mm in thickness plastic as shown in Fig. 4.1. The EJ-276G emits in the visible spectrum due to the addition of a waveshifter (Fig. 4.1). The new material has improved hardness and stability in addition to improved PSD properties from its predecessor EJ-299.

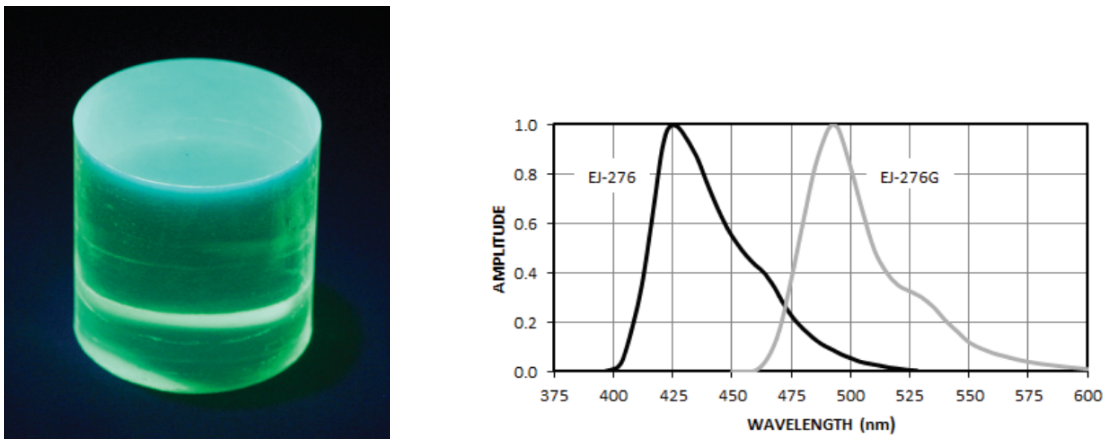

Figure 4.1: Left: EJ-276G plastic scintillator. Right: EJ-276G emission spectrum. [25]

The properties of the plastic can be found in table 4.1 [25].

Table 4.1: Main Characteristics of EJ-276G scintillator

	EJ-276G
Light Output (% Anthracene)	52
Scintillation Efficiency (photons/1 MeV e^-)	8000
Wavelength of Maximum Emission (nm)	490
No. of H Atoms per cm^3 ($\times 10^{22}$)	4.546
No. of C Atoms per cm^3 ($\times 10^{22}$)	4.906
No. of Electrons per cm^3 ($\times 10^{22}$)	3.533
Density (g/cm^3)	1.096

4.1.2 Strontium Iodide doped with Europium ($SrI_2 : Eu$)

One of the possible secondary systems for the active target at SPES can be a system well-suited for gamma spectroscopy. On that front, a promising new scintillator for this task is the Strontium Iodide doped with Europium. According to [26] it is said to be the next $LaBr_3 : Ce$ with its high energy resolution that can reach 2.8% at 662 keV. The $SrI_2 : Eu$ utilized in this work was a crystal with a cylindrical shape with dimensions 25 mm diameter x 25 mm thickness manufactured by AdvaTech UK. The crystal is shown in Fig. 4.2 while the prime properties of the crystal can be found in table 4.2 [27].

Figure 4.2: SrI_2(Eu) scintillator crystal.

Table 4.2: Properties of SrI_2(Eu) as reported by manufacturer

	SrI_2(Eu)
Light Yield (photons/keV)	115
Photoelectron Yield (% NaI(Tl))	130
Wavelength of Maximum Emission (nm)	435
Decay time (ns)	1200
Density (g/cm^3)	4.55
Effective atomic number	49

4.1.3 Thermal Neutron scintillator

The detection of thermal neutrons is an especially challenging task owed to the very low cross section of nuclear interaction with neutrons for many materials. In order to solve such conundrum, some materials are synthesized with adequate concentration of nuclei with high cross section of interaction with neutrons such as ^{6}Li, ^{10}B, etc. However, in many cases, the crystals can be fragile or toxic. To tackle these problems, a novel scintillation detector has been manufactured by Carturan et al at Legnaro National Laboratory (INFN-LNL) [29]. The scintillator consists of a ZnS:Ag scintillation powder mixed with fully enriched Lithium Tetraborate ($^{6}Li_2^{10}B_4O_7$) dispersed in a PDMS (polydimethylsiloxane) matrix. [10]. For the sake of this work, this material will be called LiBO onward.

The novel detector is synthesized by mixing fine powder of EJ-600 (ZnS:Ag) from Eljen Technology with LiBO nano particles and DMS matrix in the presence of binding agents and an inhibitor. The sample is then spread on a glass plate with the thickness of 0.5 mm. Finally, the mixture is heated in a dry oven at temperature $\sim 65°C$ for a few hours. The final product is a flexible thin layer that can be cut into any shape as shown in Fig. 4.3 [10].

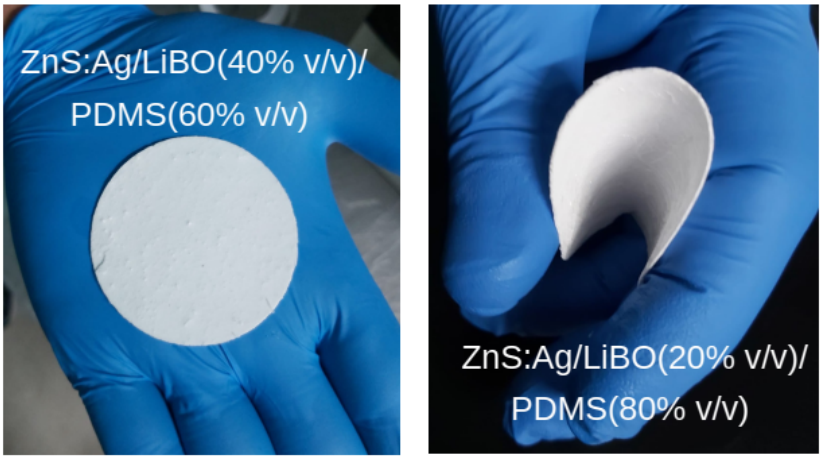

Figure 4.3: Pictures of the scintillators produced (a) LiBO(40%v/v)/PDMS and (b) LiBO(20% v/v)/PDMS [10]

Some characteristics of the LiBO can be found in table 4.3.

Table 4.3: Main Characteristics of LiBO.

	LiBO
Thickness (mm)	0.4-0.5
Light Output	9000-30000
Wavelength of Maximum Emission (nm)	450
Decay Time (ns)	200
Density (g/cm^3)	1.1-1.3

In this work, the LiBO utilized had the ratio of ZnS:Ag/LiBO (30% v/v)/PDMS(70% v/v) with ZnS(Ag):LiBO mass ratio of 2:1. Although better neutron efficiency can be obtained from higher percentage of ZnS:Ag/LiBO, at this percentage, the mechanical properties and flexibility are excellent [10].

4.2 Read-out Devices

4.2.1 Photo-multiplier tube

In this study, two photo-multiplier tubes manufactured by Hamamatsu were employed (R6233 and H6524). Fig. 4.4 shows some photographs of the devices and table 4.4 highlights their main properties [9].

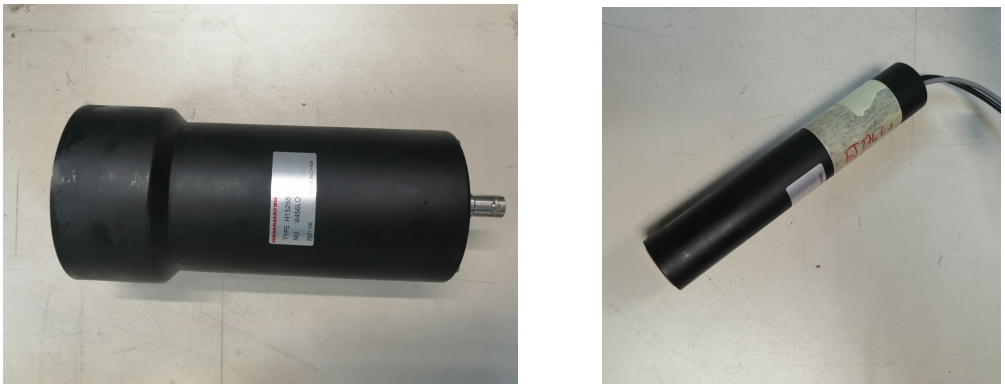

Figure 4.4: Left: Hamamatsu PMT model R6233. Right: Hamamatsu PMT model H6524.

Table 4.4: Properties of the Hamamatsu PMTs used

	R6233	**H6524**
Tube size diameter (mm)	76	23.5
Photocathode size diameter (mm)	70	19
Spectral response (nm)	300-650	
Anode to Cathode supply voltage (V)	1000	-1500
Average anode current (mA)	0.1	0.43
Gain	2.7 x 10^5	1.7 x 10^6
Rise Time (ns)	9.5	1.8
Dark Current after 30 min(Typ.) (nA)	2	3
Quantum Efficiency (%)	26 @ 420 nm	
Application	SrI2 :Eu	EJ-276/LiBO

4.2.2 Silicon Photomultiplier Array (SiPM)

In this study, a relatively new SiPM array from Hamamatsu (S14161-6050HS-04) has been utilized as the light converter for both the SrI_2 : Eu and the EJ-276G scintillator. It mainly consists of 4 x 4 matrix of single SiPMs. The main properties of this SiPM can be in table 4.5. Fig. 4.5 shows a photograph of the SiPM [9].

Table 4.5: Properties of Hamamatsu SiPM

Model	**S14161-6050HS-04**
Size	25 x 25 (mm^2)
Channels	16
Pixel pitch	50 μm
Number of pixels/channel	14331
sensitive area/channel	6 x 6 (mm^2)
Geometrical fill factor	74%
Photon detection efficiency	51% @450 nm
Breakdown voltage	38 V
Gain	2.5 x 10^6 @ 2.6V (OV)
Cross talk probability	8.5% @51% PDE & 2.6V (OV)

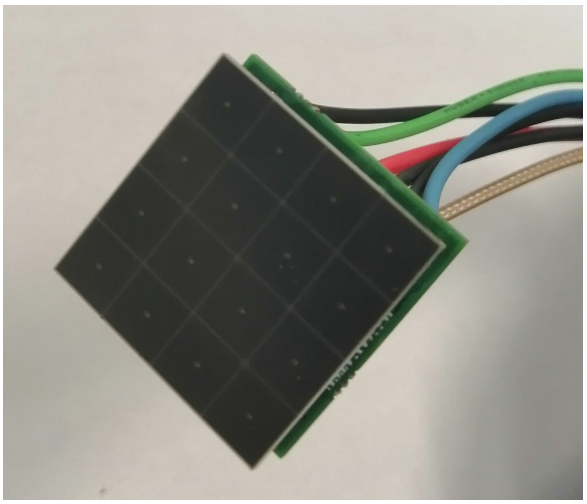

Figure 4.5: Hamamatsu S14161-6050HS-04 SiPM coupled to the readout board.

The electrical pulses of the SiPM is typically too low, hence, they require some amplification first. To do so, a circuit has been designed by the engineering team at INFN Padova. This circuit connects and powers the single SiPMs. In addition, it provides amplification and regulation of the signal that does not alter the decay time of the pulse in order to ensure the possibility of PSD. The main idea behind the circuit is that there are four sets of four channels. Each four channels are connected in parallel (one set), and the sum of their signals is connected to an operational amplifier, moreover, the outputs of the four sets coming from the four operational amplifiers are summed using another operational amplifier as can be seen in Fig. 4.6.

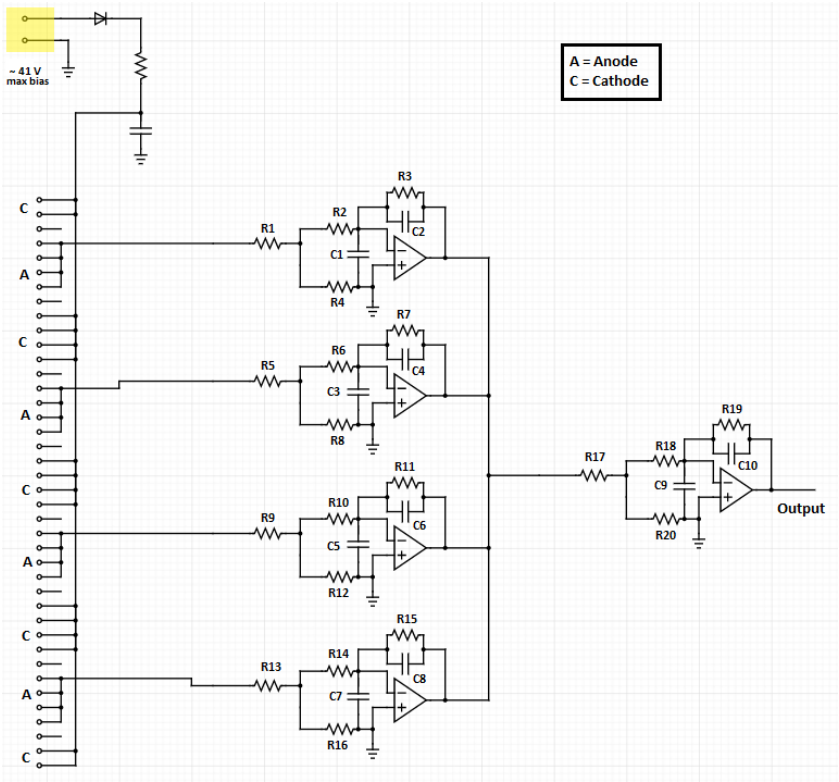

Figure 4.6: Schematic diagram of the SiPM readout board circuit.

4.3 Electronic Modules

4.3.1 Voltage supply units

The high voltage supply unit employed in this work for the operation of the PMT was the CAEN model V6533M (Fig. 4.7). It is a VME type HV power supply with 6 channels, each capable of providing up to 4 kV, 3 mA (Up to 9 W), three of them have positive polarity and the other three have negative polarity. The system is provided with a safety mechanism that warns the user in case of a difference between the programmed value of voltage and the actual value with undervoltage or overvoltage warning. Furthermore, in the case of a current that exceeds the programmed limit for overcurrent, the system shuts down after a certain (set by the user) period of time [11].

Figure 4.7: Power supply module CAEN model V6533M [11].

The voltage required for the operation of the Hamamatsu SiPM was provided by a DC power supply module from aim TTi, specifically, model MX180T (Fig. 4.8). This module contains triple output channels with multi-ranges two of which are capable of producing a DC voltage up to 180 watts with voltage ranging 10-60V and current ranging 0-6A. The third output can provide low voltage up to 18 watts with voltage and current 5.5V/3A or 12V/1.5A. The range switching function allows it to provide voltage up to 120V/3A with internal range combination for a power up to 360 watts [30].

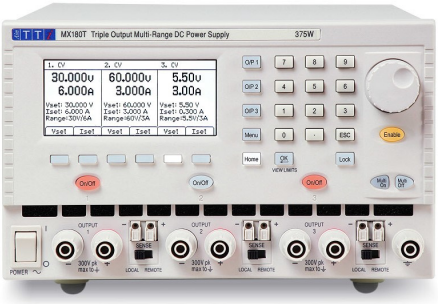

Figure 4.8: Aim TTi DC power supply model MX180T [30].

4.3.2 USB Port (Controller)

In this work, CAEN module V1718 (Fig. 4.9) was utilized to control different electronic nuclear VME modules. It is VME to USB 2.0 bridge that fills the role of VME master module that converts simple commands provided by user in to VMEbus language. Each module in the electronic chain has its own library that provides the instructions for operation. The data transfer rate of this module can reach up to 30 MB/s and can be connected to a PC via a USB connection [11].

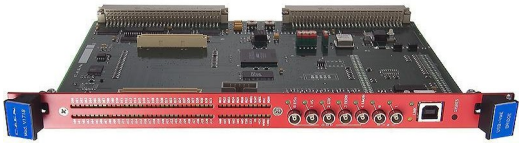

Figure 4.9: USB Port CAEN model V1718 [11].

4.3.3 USB Adapter (A4818)

The optical bridge used in this work was the CAEN A4818 USB 3.0 to CONET Adapter (Fig. 4.10). It acts as the connection between the controller and/or digitizer and the PC. The A4818 has a transfer rate of 80 MB/s via an optical fiber link from modules to the adapter. The adapter is then connected to the PC via a USB 3.1 Gen1 connection compatible with the Linux OS [11].

Figure 4.10: CAEN USB adapter model A4818. [11].

4.3.4 Digitizers

The signals obtained from the SiPM or PMT are analog signals. In order to obtain a digital signal useful for this application, a digitizer is needed. Due to the advancements in digitizers technology driven by the substantial increase in applications using detectors, modern digitizers now are capable of eliminating the need for multiple devices which greatly increases the compactness of the system and enables the conversion from analog to digital as close as possible to the detector. This was made possible due to the implementation of FPGA (Field Programmable Gate Array) which made DPP (Digital Pulse Processing possible). DPP algorithms can use the FPGA to extract vital information on-line directly from the waveform which allows the extraction of the energy, time, PSD parameter, etc. These signals can aid the future adjustments to the algorithm leading to improved data collection [5] [31].

The operation principle of the waveform digitizer can be summed up in the following

- Analog to digital conversion continuously takes place and events that surpass the threshold causes a trigger.
- When a trigger takes place, a set number of samples (determined by acquisition window) are saved into the memory buffer.
- If another trigger simultaneously takes place, the same process will take place in another buffer. This allows multiple events to be recorded simultaneously which removes the dead-time of the digitizer (given enough memory) enabling the proper acquisition of high counting rate.

The algorithm programmed in the FPGA in this work to discriminate between the neutrons and gamma rays depends on the ratio between charge collected within two fixed gates as shown in equation 4.1 and demonstrated in Fig. 4.11.

$$\mathrm{PSD} = \frac{\mathrm{Q_{long}} - \mathrm{Q_{short}}}{\mathrm{Q_{long}}} = \frac{\mathrm{Q_{tail}}}{\mathrm{Q_{total}}} \tag{4.1}$$

Where $\mathrm{Q_{long}}$ is the charge integrated along a long gate and $\mathrm{Q_{short}}$ is the charge integrated along a short gate.
For each waveform, **n** samples are collected. From these samples the baseline, partial charge integration ($\mathrm{Q_{short}}$), and total charge integration ($\mathrm{Q_{long}}$) can be determined. The baseline line is the input level that minimizes the noise and fluctuations. The charge integration represents the summing of all the charges of all the samples residing within the window. The baseline is subtracted from the integration. The pre-gate which represents trigger position alongside the short and long integration gates are typically adjusted online and offline to improve the results.

In this work, two digitizers were used, the first was CAEN DT5725 which is a desktop digitizer with 8 input channels, CAEN V1730 which is a VME digitizer with the capability of double the sampling rate and channels. Both digitizers are illustrated in Fig. 4.12 and their main properties can be found in table 4.6.

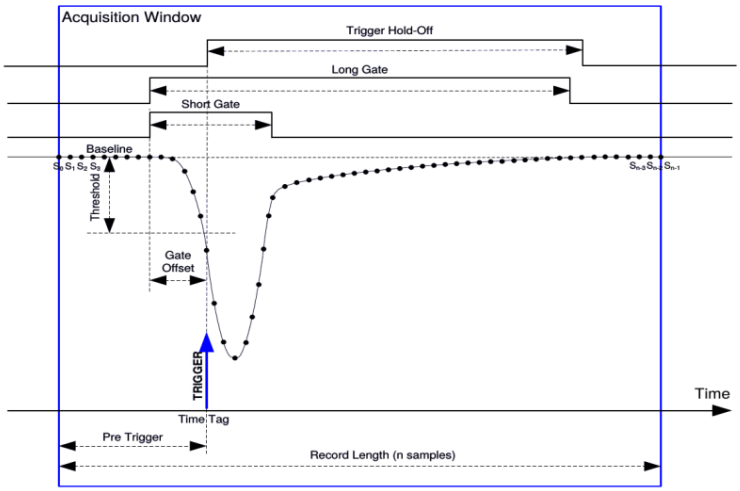

Figure 4.11: Illustration of the waveform of a digitized signal and its components [32].

Figure 4.12: Left: CAEN DT5725 digitizer. Right: CAEN V1730 digitizer [11].

Table 4.6: Main characteristics of CAEN DT5725 and V1730 digitizers [11].

	DT5725	**V1730**
Analog input	8 channels (50Ω impedance)	16 channels (50Ω impedance)
Scale voltage range	0.5 or 2 Vpp	0.5 or 2 Vpp
Sample rate	250 MS/s	500 MS/s
ADC resolution	14 Bits	14 Bits
Connectivity	USB and optical Link Controller	Optical Link Controller
Power consumption	2 A @ 12 V	8.2 A @ +5 V / 840 mA @ +12 V

4.4 Radioactive sources

In order to calibrate both the plastic and the SrI_2 : Eu scintillators, it is necessary to use radioactive sources that emit gamma radiation and neutrons. In the case of the plastic scintillator, to study the discrimination capabilities of each setup, a measurement had to be taken with a neutron/gamma source. In this case, two neutron sources were deployed on two different occasions ^{241}AmBe, and ^{252}Cf. The ^{241}AmBe neutron source is a neutron source of that utilizes the reaction (α, n) reaction, in

this particular case, the ^{241}Am decays to ^{237Np} (100%) by emitting an alpha particle with a Q-value of 5.49 MeV. This alpha is captured by a ^{9}Be target via the channel $^{9}\mathrm{Be}(\alpha, \mathrm{n})^{13}\mathrm{C}*$ where the excited Carbon decays to ^{12}C by emitting a neutron and gamma of energy 4.4 MeV.The ^{241}AmBe used had a neutron intensity of 2.14×10^{5} N/s (in July 2003). The second neutron source was Californium (^{252}Cf) source which has two main emissions. The ^{252}Cf decay can emit alpha particles (96.91%) and it can decay by spontaneous fission (3.09%) where the fission process produces multiple fast neutrons with energies in the range of MeV (peaked around (0.5-1 MeV) in addition to high energy prompt gamma rays. The energy spectrum of the fission neutrons follows

$$\frac{\mathrm{dN}}{\mathrm{dE}} = \sqrt{\mathrm{E}}\mathrm{e}^{-\frac{\mathrm{E}}{\mathrm{T}}} \tag{4.2}$$

Where the constant **T** for ^{252}Cf is 1.3 MeV [12].
The prime properties of the ^{252}Cf source as well as the different gamma sources utilized in this work can be seen in table 4.7 [12].

Table 4.7: Information of the radioactive sources used [33].

Source	**Activity (kBq)**	**Half-life (year)**	**Date**	**Emission**
^{60}Co	383	5.2711	01/06/2015	gamma
^{22}Na	384	2.6029	01/06/2015	
^{137}Cs	386	30.05	01/06/2015	
^{133}Ba	405	10.539	01/06/2015	
^{252}Cf	2×10^{3}(*2.6×10^{4})	2.647	15/02/2014	neutron-gamma
^{241}AmBe	3.7×10^{6}(*2×10^{5})	432.6	10/02/2003	neutron-gamma

Note: * represents the neutron emission rate in neutrons/second.

4.5 Proton beam (LABEC)

In order find the proton light output function of the EJ-276G scintillator, measurements using a proton beam of different energies were performed at the INFN ion beam laboratory LABEC at Florence, Italy (Fig. 4.13). The facility contains a 3 MV TANDEM connected to a switching magnets and multiple beam lines. The proton beam produced, was extracted out of beamline at +45° with energy of ∼5 MeV and was collimated in a diameter of ∼0.5 mm. The beam has to pass through a 200 nm membrane of Si_3N_4 to be extracted to ambient pressure, then passes through 10 mm of air to reach the setup [34]. Different energies were obtained by attenuating this beam using first larger distance from beam exit (more air thickness), then different thicknesses of Upilex foil. The energies of protons used can be found in table 4.8.

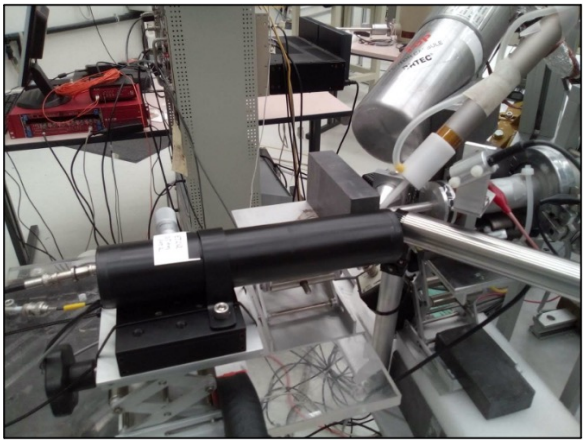

Figure 4.13: Experimental setup at the LABEC laboratory.

Table 4.8: Energies of Proton beam utilized (energies obtained from SRIM).

Energy (MeV)	**En. strag.(σ_E)** (MeV)	**Layers between beam and detector**
4.910	0.01	200 nm Si_3N_4 + 10 mm air
3.985	0.037	200 nm Si_3N_4 + 110 mm air
2.919	0.054	200 nm Si_3N_4 + 110 mm air + 75 μm Upilex-S
2.013	0.085	200 nm Si_3N_4 + 110 mm air + 125 μm Upilex-S
1.414	0.105	200 nm Si_3N_4 + 110 mm air + 150 μm Upilex-S

4.6 Fast Neutron Field (CN accelerator)

To study the scintillator response under fast neutron field, the accelerator at the CN facility of Legnaro National Laboratories (LNL) was used. The monoenergetic neutron field was produced via the reaction $^7Li(p,n)^7Be$, where a pulsed beam of protons was produced by the Van de Graaff accelerator and set to collide with a ^7LiF target of thickness 700 $\mu g/cm^2$. The proton beam had energy of 5 MeV (3 MHz rep rate with ∼2 ns pulse width). The detector was placed at 0° and 90° which yielded neutrons of energies 3.3 MeV and 2.3 MeV respectively with variation in the neutron energy of ∼0.06 MeV within 2° [35].

4.7 Data acquisition system (DAQ)

A DAQ is a software that reads and analyzes signals generated by nuclear detectors. Additionally, it can be used to control the setup parameters such as digitizer configuration, high voltage, and display of spectra for the online analysis. The DAQ used for this work is called **A**cquisition and **B**roadcast of **C**ollected **D**ata (ABCD) data acquisition system. This DAQ divides different functionalities into processes ("servers") that can run separately which enables the capability of splitting the hardware load of different processes to different computers. The servers were developed in C99 and C++11 while auxiliary tools and scripts were written in Python. ABCD can be run via a GUI launched on the browser and different settings can be controlled by the python scripts launched through the terminal. Different processes can be launched through different servers as follows

- Control over the digitizer acquisition configuration and displays the counting rate of each channel.
- Control of high voltage (HV) for the PMT.
- Saving of data and type of files generated (raw, waveform, and event).
- Displaying waveform and 1D histograms of energy and PSD.

The systems supports the operation and analysis of multiple digitizers simultaneously using different servers [20] [21].

4.8 Geant4 Monte Carlo Simulation

4.8.1 Monte Carlo Method

Developed in the late 1940s in Los Alamos National Laboratories [36], the Monte Carlo method relies on the utilization of a substantial number of reoccurring random sampling in order to solve a problem with a probability distribution function. This method, in addition to being faster in some cases to solve analytical problems (due to the utilization of fast computers), can solve problems with no analytical

solution. Through the use of Monte Carlo algorithms, a plethora of fields such as economics, natural sciences, engineering, and social sciences have been able to solve problems with multiple degrees of freedom easily [37].

The Monte Carlo method depends on the knowledge of microscopic interactions that can be modeled in order to give the macroscopic behavior [37]. Thus, it has been utilized in the field of science to provide proof of concepts, confirm experimental results, or test out different configurations. For example, physical quantities such as the momentum, trajectory, energy loss, and decay can be modeled using multiple types of Monte Carlo simulations by knowing the cross sections of distinct interactions at various energies for different particles such as pair-production, or photoelectric effect. This can be done by many programs and frameworks such as SRIM, Geant4, LISE++, and PYTHIA.

4.8.2 GEANT4 simulation toolkit

GEANT4 stands for **GE**ometry **AN**d **T**racking. It is a framework developed by a large team of several fields at CERN using the programming language C++. It is meant to serve as the successor of GEANT3 which worked with Fortran instead. GEANT4 is comprised of multiple libraries containing functions and classes with models and tables governing all aspects of simulation such as geometry of the system, materials involved, fundamentals particles of interest, particles or photons for the beam, various physics phenomena to be included for the interaction, tracking of the particles through the material with or without external electric or magnetic field, and more [38].

The procedure followed to create a GEANT4 simulation is as follows

- Creation of the C++ classes needed that define the processes mentioned above to be utilized by the simulation (geometry, primary particles, physics models, etc).
- Initializing these classes in the **main** class.
- Compile the libraries using *cmake*.

In this work, the **EJ-276G** scintillator was simulated and all the crucial classes were deployed as explained below.

Detector construction

For the definition of the main properties of the geometry, materials, and orientation of the detector, the **G4VUserDetectorConstruction** class was exploited. Inside this class, the G4Box and G4Tubs classes which inherit from the G4Solid class were used to define the **physical volume** of the world and the detector respectively. The dimensions of the world volume were 200 cm x 200 cm x 200 cm while the detector had a cylindrical shape with dimensions 25.4 mm diameter x 25.4 mm thickness. Following, the classes G4Element and G4Material were used to define the elements (C, H) and the EJ-276G material respectively. The density of the material as well as the concentrations of each element were obtained from [25] [39]. Afterwards, the materials and solid dimensions attributes were attached to a **logical volume** using G4LogicalVolume class where the visual attributes were added during this step. Subsequently, the physical volume of the detector was placed inside the world volume with no rotation and at distance 25 cm from the center of the world box by making use of G4PVPlacement class. Finally, the logical volume of the detector was assigned as a sensitive volume. Fig. 4.14 clarifies the setup of the simulation.

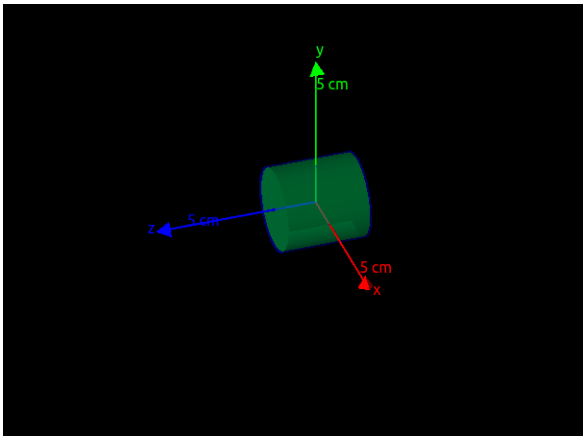

Figure 4.14: Geant4 simulation of the EJ-276G scintillator

Primary generator

In order to define the primary particles or photons impinging on the detector and all their properties, the class **G4VUserPrimaryGeneratorAction** was implemented. When no angular distribution for the photons was needed, G4ParticleGun was used. In case of cone shaped distribution, G4GeneralParticleSource (GPS) class was utilized instead. The GPS class contains many methods that were invoked via commands in a macro file to assume a cone shape covering the solid angle of the scintillator.

Physics List

The physics invoked by the simulation was defined via the class **G4VModularPhysicsList** where in the case of photons, the library **G4EmLivermorePhysics** was utilized while in the case of the neutrons the library **G4HadronPhysicsQGSP_BERT_HP** was used instead. G4EmLivermorePhysics contain all the essential interactions for gamma rays such as photoelectric effect, the Compton scattering, the Rayleigh scattering, and the pair production. On the other hand, the G4HadronPhysicsQGSP_BERT_HP library contained elastic collision, inelastic collision, neutron capture, and fission. It is suitable for neutron energies less than 10 GeV as well as the ability to transport neutrons down to thermal energies [40].

Tally of data

The logical volume of the detector was set as a sensitive volume. In order to collect information about the interaction between neutrons (or gamma rays) and the scintillation volume, the following classes were invoked

- **G4UserRunAction**: Inside this class the run is initialized where the histograms and tuples are created and saved.
- **G4UserSteppingAction**: The energy lost by the neutron (or photon) as well as that of all the secondary particles produced by it are obtained in this class. A filtration is done to exclusively record information of relevant particles. To illustrate, in the case of the neutron field, only the kinetic energy of the recoil protons is recorded as it is responsible for the majority of light produced due to the higher cross section of scattering between the neutrons and hydrogen.
- **G4UserEventAction**: Inside which the overall physical quantities arising from the interactions of a single neutron or photon (an event) with the detector material are recorded in the tuples and histograms.

Chapter 5

Results and Discussion

The characterization of both the organic and inorganic detectors is discussed in this chapter alongside the determination of the discrimination capabilities of the organic detector EJ-276G as a standalone detector as well as a composite detector when coupled with the LiBO.

5.1 Plastic Scintillator (EJ-276G)

The characterization of the organic scintillator can be difficult as it does not have distinct energy peaks, instead, it has Compton distributions. The calibration was done using ^{137}Cs and ^{22}Na sources. Using equation 2.19, the values of the gamma-ray energy peaks of ^{137}Cs and ^{22}Na are tabulated alongside their corresponding Compton edge energies in table 5.1.

Table 5.1: Gamma-ray energies and Compton edges of ^{137}Cs and ^{22}Na.

Source	Gamma-ray energy (keV)	Compton edge (keV)
^{137}Cs	661.66	477.34
^{22}Na	511	340.67
^{22}Na	1274.54	1061.71

5.1.1 Energy Calibration

The calibration runs were done using the Hamamatsu H6524 PMT and CAEN V1730 digitizer (see Fig. 5.1), where the channel corresponding to the Compton edge energy was assumed to be 80% of the maximum of the Compton edge distribution following the same methodology of [41]. Fig. 5.2 shows the shape of the ^{137}Cs spectrum for the EJ-276G with the arrow indicating 80% of the max intensity.

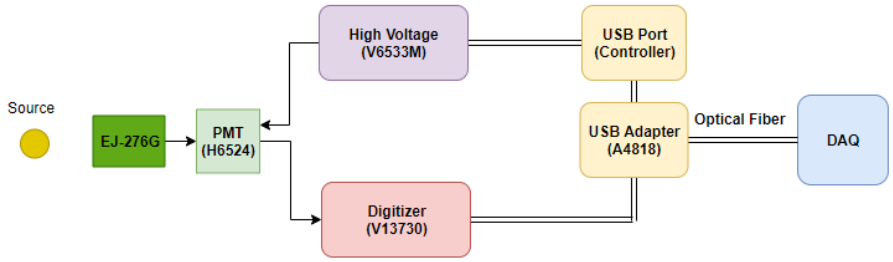

Figure 5.1: Diagram of the experimental setup of EJ-276G scintillator.

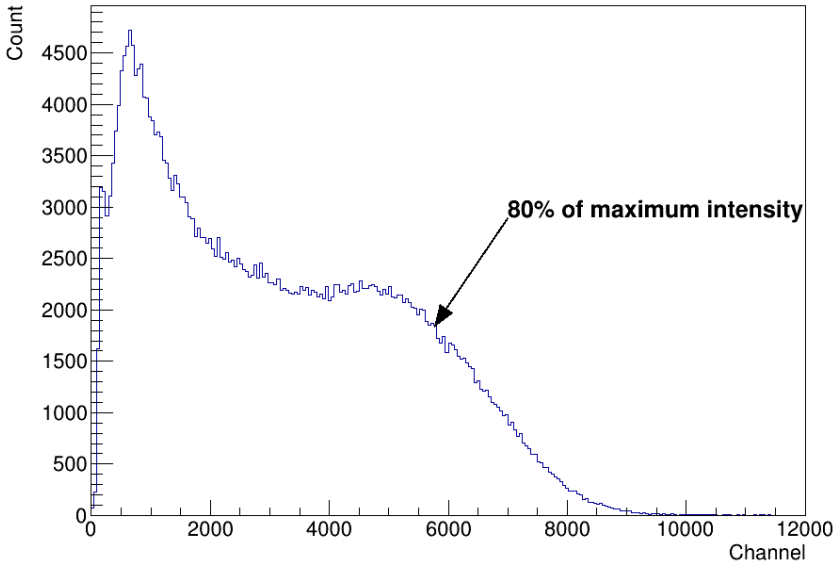

Figure 5.2: ^{137}Cs Spectrum with the EJ-276G.

Fig. 5.3 highlights the energy calibration together with a linear fit.

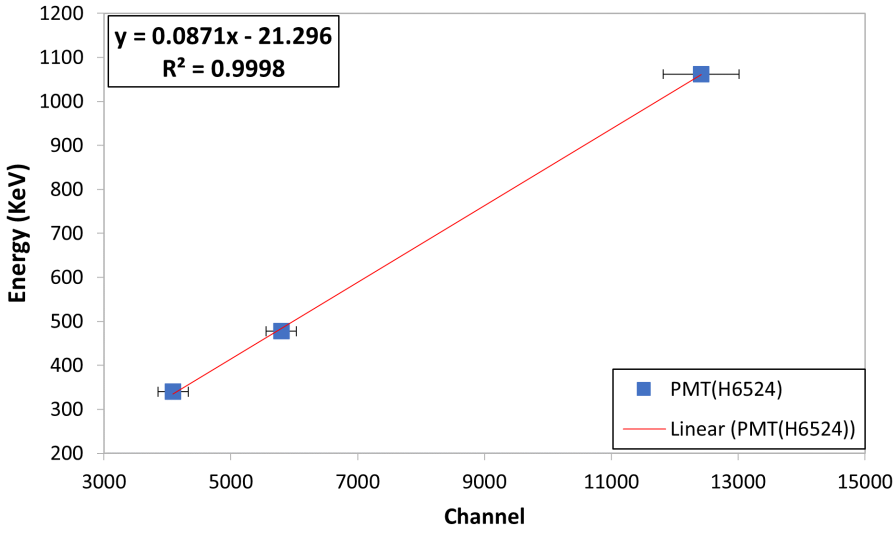

Figure 5.3: Calibration of EJ-276G using a linear fit.

Fig. 5.4 shows the ^{137}Cs and ^{22}Na spectra of calibrated.

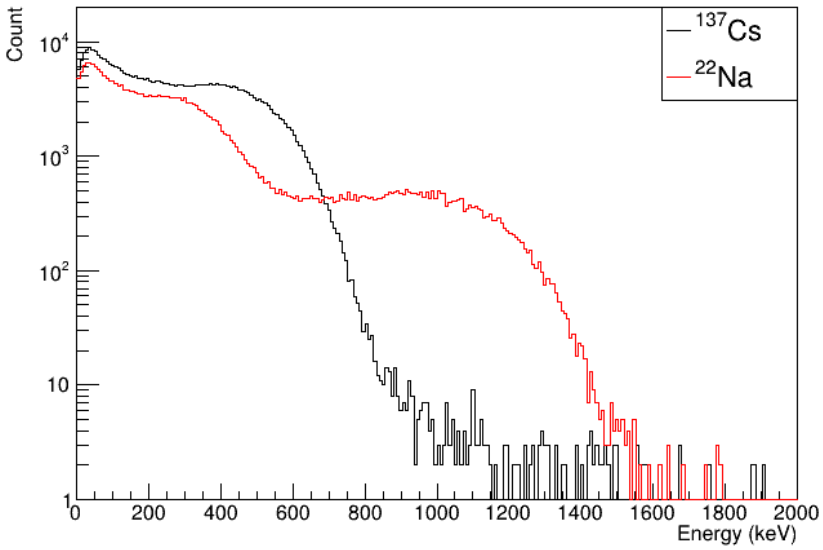

Figure 5.4: Post calibration^{137}Cs and ^{22}Na spectra.

5.1.2 Neutron-Gamma Discrimination

Following the energy calibration process, the discrimination between the gamma rays and neutrons must be determined. As mentioned in chapter 2, this is done using the FoM parameter. Fig. 5.5 presents a 2D histogram with the X-axis filled with the light output and the Y-axis filled with the PSD parameter which is computed using equation 4.1. This is done by taking a projection of the y-axis for a certain range of the x-axis , usually around 1 MeV as shown in Fig. 5.5(left), and fitting two Gaussians as shown in Fig. 5.5(right). In order to check the optimal short and long integration gates, the same process is repeated with different values in order to find the short and long gate values that maximize the FoM. The optimal gates were found to be **1400 ns** for the long gate and **84 ns** for the short gate and the FoM obtained was ($\mathbf{0.96 \pm 0.06}$).

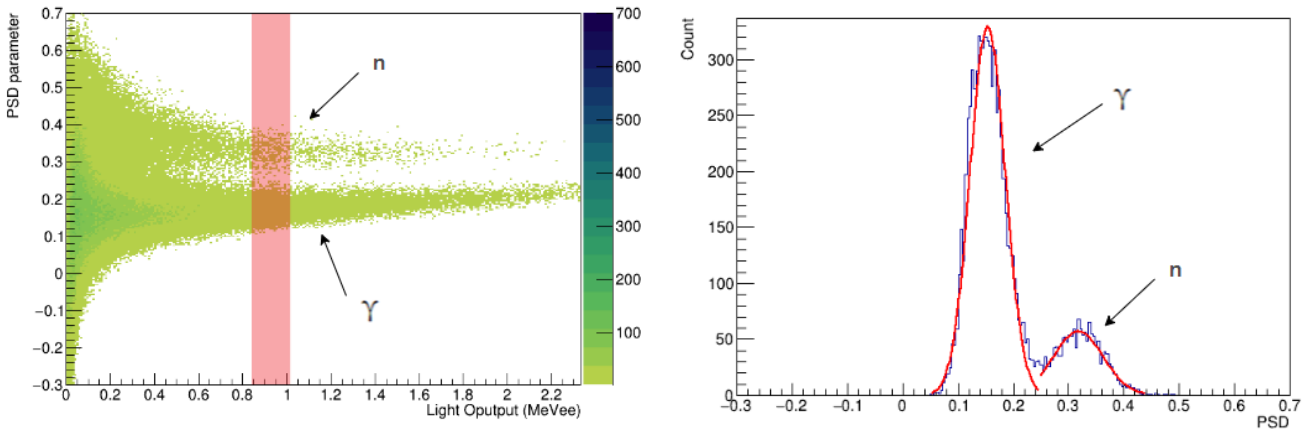

Figure 5.5: Left: Light Output-PSD 2D Histogram. Right: Projection of PSD with Gaussian fit of gamma peak and fast neutron peak.

In Fig. 5.6, it can be seen that the value of FoM increases with increasing the width of the short gate, however, there is a maximum value (84 ns) beyond which the FoM decreases as the width of the gate becomes large enough that the difference between the shape of the pulse arising from neutron and that from gamma become obsolete. Furthermore, a steady growth in the value of the FoM with

increasing the width of the long gate can be observed, non the less, a long gate of 1400 ns was chosen as the full range of the waveform is 2048 ns and integrating more than 1400 ns means that some of the background will be included as well.

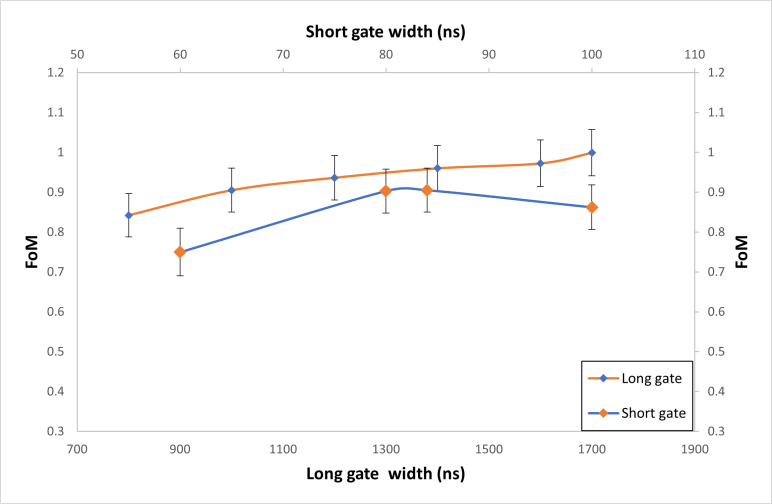

Figure 5.6: FoM Vs short and long gate widths

Finally, to check the effect of the light output threshold on the FoM, similar process to Fig. 5.6 was done. Nonetheless, projection of the Y-axis was done from $\sim$ 0.2 MeVee until $\sim$2.3 MeVee with the light output threshold increasing by steps of $\sim$0.2 MeVee and number of bins included in the projection reduced by 25 each step. It can be seen in Fig. 5.7 that as the threshold is increased, the FoM gradually increases as well. This can give an insight of the expected FoM at each energy threshold. To elaborate, for applications with fast neutrons of high energies, a high threshold can be used to improve the neutron-gamma discrimination.

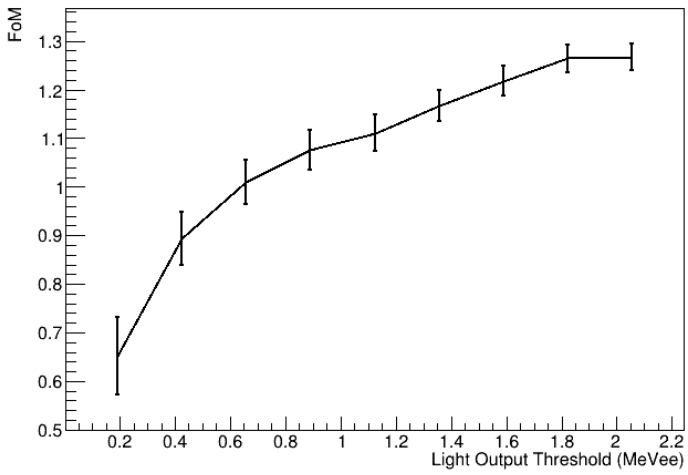

Figure 5.7: FoM Vs Light Output Threshold.

5.1.3 Proton Light Output Function

In order to determine the light output function of the EJ-276G scintillator, the proton beam data from LABEC was utilized. Each spectrum was fit using a Gaussian function and the mean and standard deviation values provided a point in the graph of the proton light output function. As shown in Fig. 5.8, the spectrum of each proton energy can be seen with each peak shifting to the left as the energy of the proton decreases.

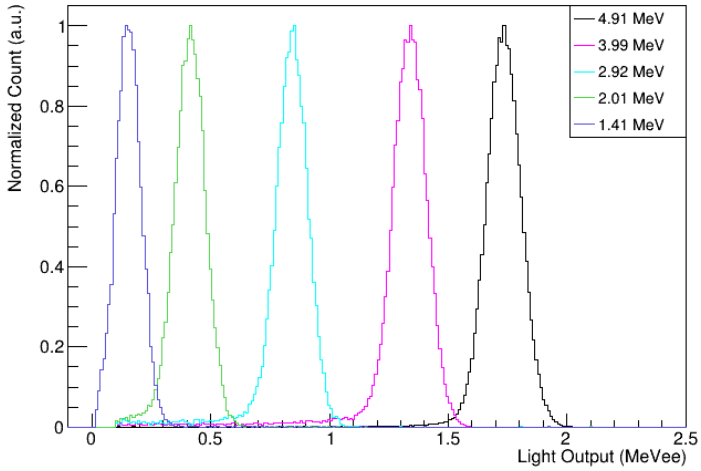

Figure 5.8: Spectra of Proton beam at LABEC normalized to their maximum value.

Subsequently, the data points were fit using three different fitting functions as shown in Fig. 5.9.

Birk's formula

In this case, the Birk's formula (equation 2.2) was used with the energy loss function initially obtained by using a power fit on $\frac{dE}{dx}$ obtained from SRIM [42] for the material of the scintillator with a proton beam within the same energy range (1-5 MeV). This fit did not provide the best results given the data available. The next step was to try the Ziegler-Anderson formula, highlighted in equation 5.1 for the energy loss function as suggested by [43](equation and parameters taken from [44]), the outcome did not significantly improve. This led to the need to try another fitting formula. The fitting parameters can be found in table 5.2.

$$\begin{aligned} \frac{1}{S_e} &= \frac{1}{S_{LOW}} + \frac{1}{S_{HIGH}} \\ S_{LOW} &= A_1 E^{A_2} + A_3 E^{A_4} \\ S_{HIGH} &= \frac{A_5 \ln(\frac{A_6}{E} + A_7 E)}{E^{A_8}} \end{aligned} \tag{5.1}$$

Table 5.2: Fitting parameters for Birk's function.

	S	**Kb**	**Reduced χ^2**
SRIM power fit	0.70 ± 0.05	6.94±0.46	2.52
Ziegler-Anderson	0.12±0.01	0.41± 0.02	3.01

Semi-empirical formula

In this scenario, the formula shown in equation 5.2 was utilized [45]. The fitting parameters can be shown in table 5.3 while Fig.5.9 demonstrates the fit. This result had improved reduced chi square of **1.12** and the fit could match the data points better, accordingly, these fitting parameters were employed for later studies.

$$L(E_p) = AE_p - B(1 - e^{-CE_p^D}) \tag{5.2}$$

Table 5.3: Fitted parameters of the light output curves from this work and liquid scintillators from [46]

Detector	Detector size (mm x mm)	A (MeVee/MeV)	B (MeVee)	C ($MeVee^{-1}$)	D
EJ-276G (this work)	**25.4 x 25.4**	**0.60±0.05**	**1.28±0.20**	**0.50±0.29**	**1 (fixed)**
EJ-299-33 [46]	**76.2 x 76.2**	**0.75**	**3.2**	**0.22**	**1 (fixed)**

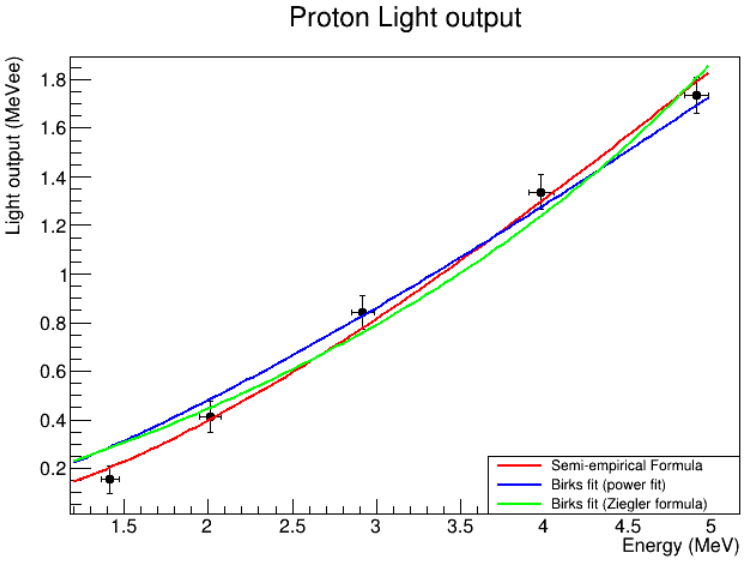

Figure 5.9: Light output fit for data from protons.

5.1.4 Response to mono-energetic fast neutrons

Mono-energetic fast neutrons data was obtained from the Van de Graaff accelerator in LNL. The setup of the experiment is shown in Fig. 5.10. Two measurements were performed with the detector placed at 90° (energy of 2.3 MeV) and at 0° (energy 3.3 MeV) with respect to beam direction.

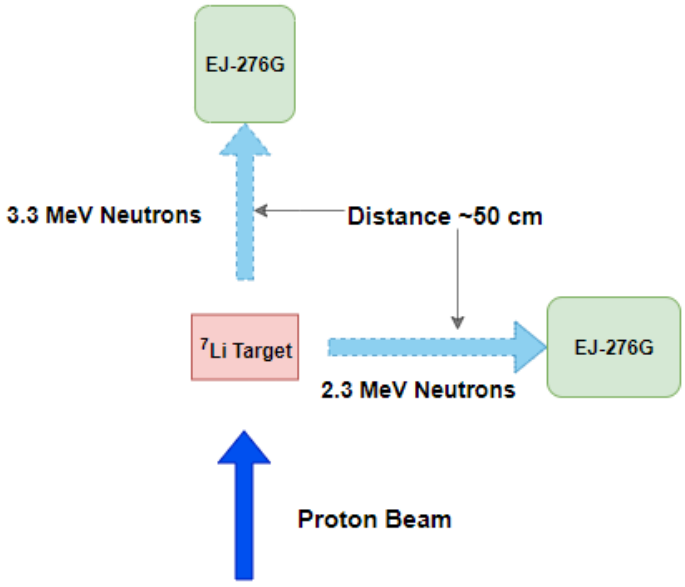

Figure 5.10: Schematic diagram of the setup in the Van de Graaff accelerator.

To obtain the light output at these energies, the methodology of [45] was followed. Initially, fast neutron events were selected from the psd-light output 2D histogram using a TCut as shown in Fig. 5.11. Subsequently, these neutron events were put in a separate histogram and the numerical derivative of the data in that histogram was obtained and inverted (to simplify the fitting process). Typically, the first minimum in the derivative represents the multiple scattering events while the second minimum is correlated to the maximum energy deposited by the recoil protons, however, due to the small size of the scintillator only the recoil protons peak appeared. A Gaussian fit was performed to that peak and the light output was determined. The process can be highlighted in figures 5.11 and 5.12. It can be noted in Fig. 5.13 that the light output obtained from these two measurements deviates from the fit obtained for the proton light output function. In the case of the 2.3 MeV, the deviation is more pronounced than in the case of 3.3 MeV. A possible explanation is that the proton beam deposit almost locally near the face of the scintillator and all the produced light would be attenuated by the same amount. Unlike the neutrons that can travel inside the scintillator leading to the creation of the everywhere inside the scintillator.

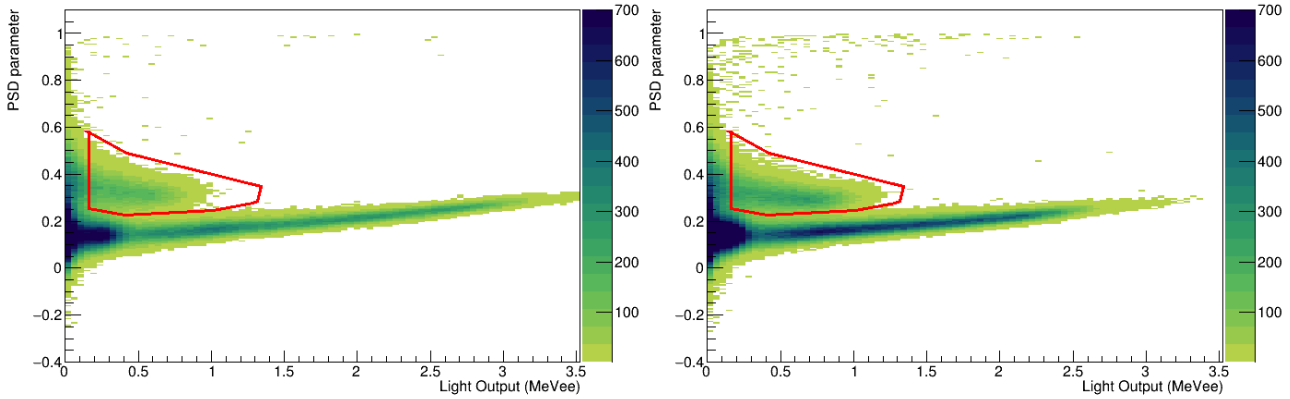

Figure 5.11: Left: light output-PSD 2D histogram of EJ-276G at 90°. Right: light output-PSD 2D histogram of EJ-276G at 0°.

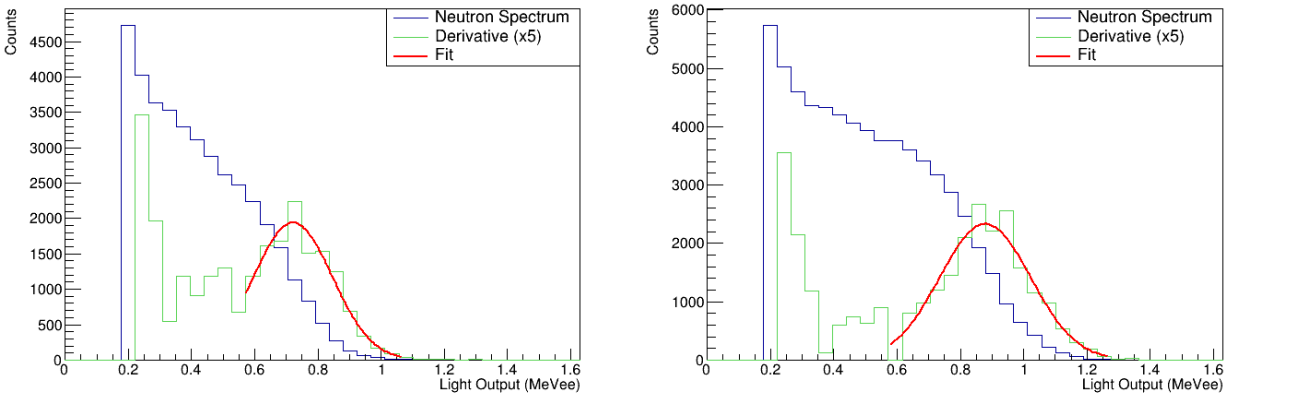

Figure 5.12: Left: light output spectrum of neutrons from the TCut projection with Gaussian fit of the numerical derivative for neutrons at 90°. Right: light output spectrum of neutrons from the TCut projection with Gaussian fit of the numerical derivative for neutrons at 0°.

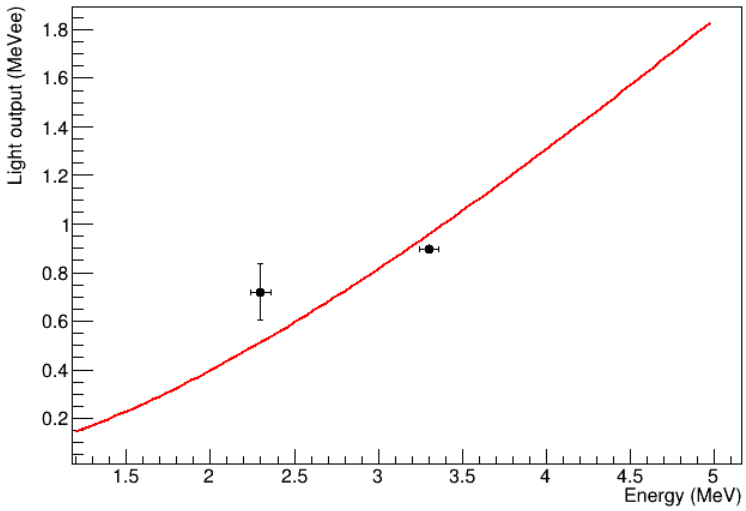

Figure 5.13: Light output of recoil protons produced by neutron field of energy 2.3, 3.3 MeV from Van de Graaff accelerator with light output function.

Comparison with Monte Carlo Simulations

To gain more insight of these results, a GEANT4 simulation was performed using a mono-energetic neutron field. The two runs were performed each with a mono-energetic neutron field with the shape of a cone with solid angle 0.008 sr as can be seen in Fig. 5.14.

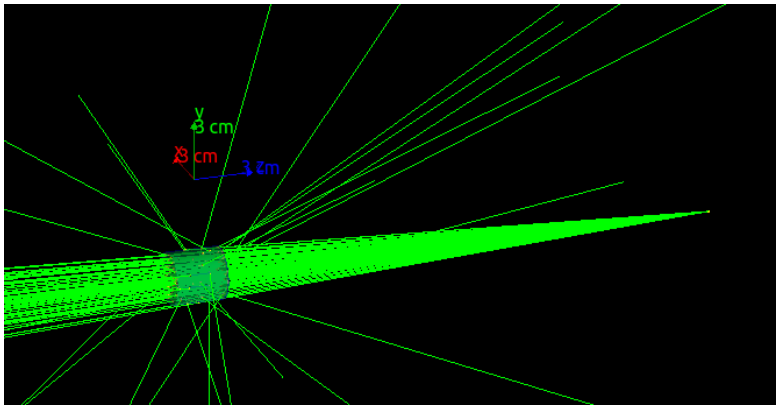

Figure 5.14: GEANT4 simulation of the response of the EJ-276G scintillator using mono-energetic fast neutron field.

The kinetic energy of the recoil protons was converted into light using the light output function obtained from the semi-empirical formula fit. The spectrum obtained from the simulation of each energy was plotted with that of the experimental results for comparison, shown in Fig. 5.15. It it notable that the discrepancy between the simulated spectrum and the experimental spectrum is more extreme for the 2.3 MeV. This can probably be attributed to the deviation from the fit mentioned above.

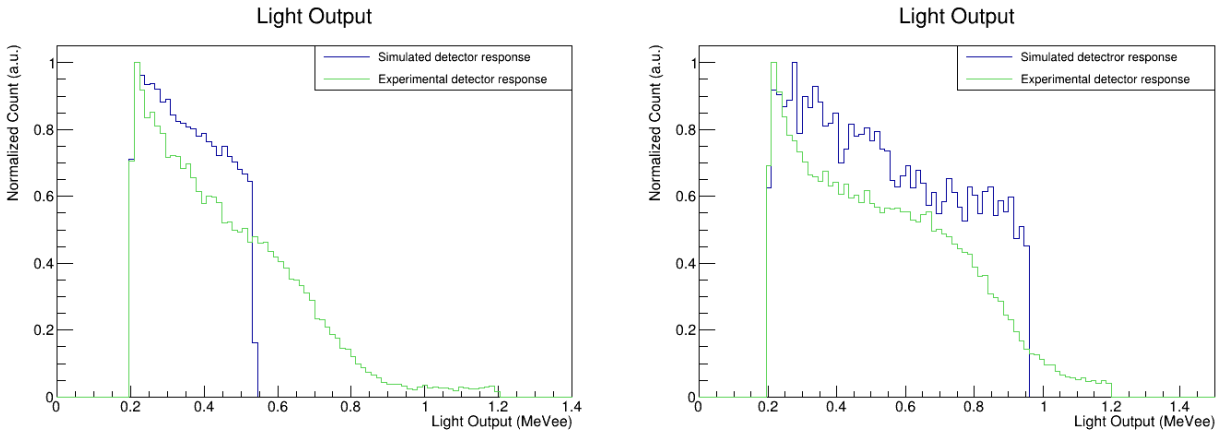

Figure 5.15: Left: Detector response for neutrons at 90° experimental and simulated. Right: Detector response for neutrons at 0° experimental and simulated.

5.1.5 Gamma and Fast Neutron Efficiencies

Gamma Efficiency

Initially, a source of gamma ray photons was implemented with energy of 50 keV and the intrinsic gamma efficiency was computed. Subsequently, the energy was increased by steps of 100 keV up to 3 MeV and the efficiencies were computed. Finally, the efficiency was plotted against the initial energy of the gamma photons. Three thresholds were considered 1 keV(almost no threshold), 50 keV, and 100 keV (Fig. 5.16). The efficiency of relevance in this case is that of the gamma photon energy 662 keV of the ^{137}Cs. The efficiency at this energy with threshold of 100 keV was found to be 13.175% which when compared to the experimental intrinsic efficiency of **11.913%** at the same threshold, has a discrepancy of only ∼**10%**.

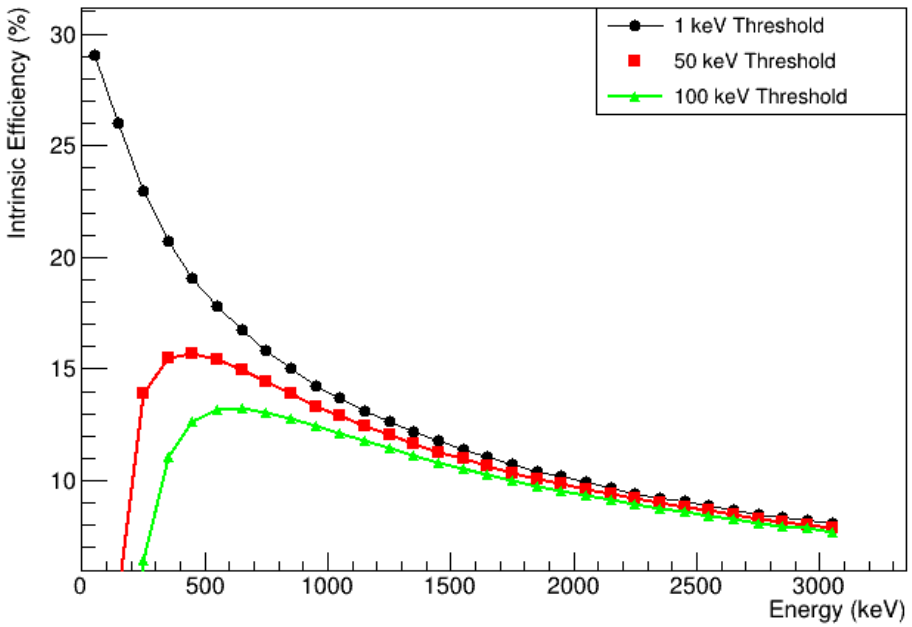

Figure 5.16: GEANT4 simulation of the EJ-276G scintillator using 10^7 gamma rays.

Efficiency using Americium Beryllium Source

Following the initial simulation, the primary particles and physics utilized were changed to accommodate for a simulation with an ^{241}AmBe source placed 25 cm away from the detector as shown in Fig. 5.17. The goal was to compute the intrinsic efficiency of the EJ-276G and verify the simulation with experimental results from the measurement. The run was 10^6 neutrons with energies of the ^{241}AmBe neutron spectrum and angular distribution of the solid angle of the detector. The intrinsic efficiency with the simulation with a threshold of 300 keV was found to be $\sim 7.8\%$ while the experimental value of the intrinsic efficiency at the same threshold was 9.4%, thus, the simulation had a discrepancy of 18.6% from the experimental value which is within the uncertainty of the activity of the source.

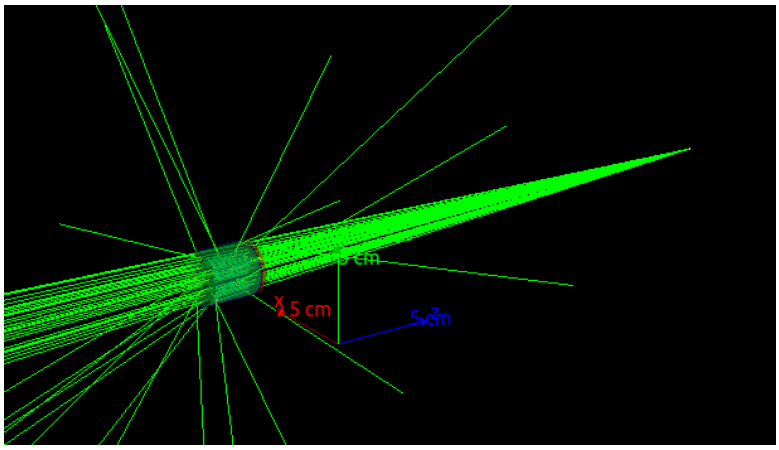

Figure 5.17: GEANT4 simulation of the EJ-276G scintillator with ^{241}AmBe source.

Fast Neutron Efficiency

Finally, the primary particles were changed once more to accommodate for a mono energetic neutron simulation. Several simulations were made with mono-energetic neutrons of energies ranging 1-10.5 MeV with steps of 0.5 MeV. Subsequently, the neutron efficiency was computed, and plotted as can be seen in Fig. 5.18.

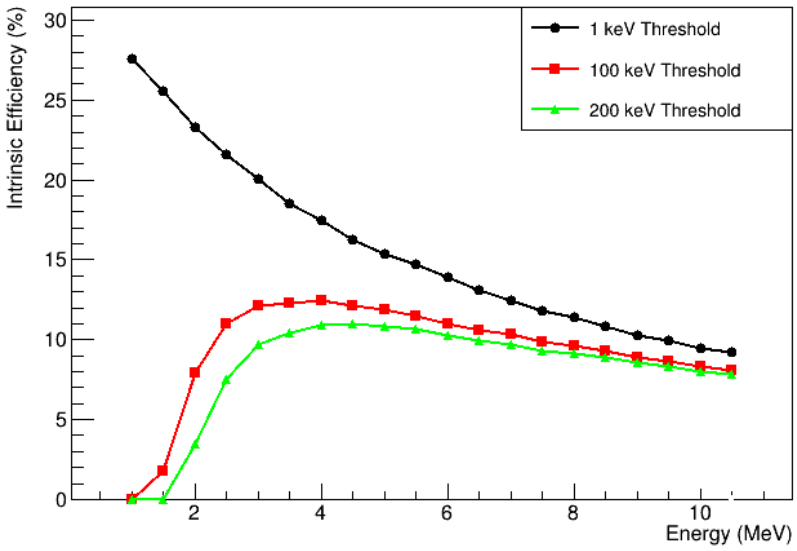

Figure 5.18: Intrinsic neutron efficiency of EJ-276G simulated with GEANT4.

5.2 Strontium Iodide doped with Europium

To begin the characterization process and to be able to compare between the performance of the SrI_2 : Eu detector when coupled with a PMT vs the SiPM, it was essential to determine the optimal operating voltage which is done by obtaining measurements with a ^{137}Cs source using different HV in case of the PMT, and in case of the SiPM using a bias voltage greater than that of the breakdown voltage. Following this step an energy calibration is performed using different radioactive gamma sources. Finally, after applying the calibration, the resolution as a function energy is determined through the measurements of different radioactive sources of different energy peaks.

5.2.1 Coupled to PMT

A schematic diagram of the setup of the SrI_2 : Eu can be shown in Fig. 5.19. Since the dimensions of the PMT were substantially larger than that of the crystal (more than double the size), the coupled system was placed inside a black box and covered with a thick black cover to prevent light from entering the PMT and causing noise or fake signals.

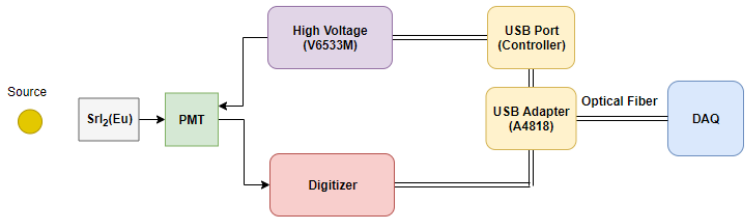

Figure 5.19: Block diagram of the experimental setup of SrI_2 : Eu with PMT.

Optimal voltage calibration and gate optimization

To get the optimal bias voltage, a ^{137}Cs source was used. The HV applied to the PMT was varied from 800 V up to 1300 V in steps of 100 V (5.4), the high voltage corresponding to the best resolution was found to be **1200 V**.

Table 5.4: HV Optimization for SrI_2 : Eu using PMT

HV(V)	Centroid	FWHM	Resolution(%)
800	2033.30	194.05	9.54
900	4091.72	249.97	6.11
1000	7602.17	399.07	5.25
1050	10069.52	468.92	4.66
1100	13179.87	640.41	4.86
1200	**20977.69**	**923.38**	**4.40**
1300	32611.61	1452.58	4.45

Following the determination of the optimal operating voltage, the optimization of the charge integration gate was done to determine the value that results in the best energy resolution. In this particular situation, the gate varied is the long integration gate only for the whole waveform because the SrI_2 : Eu is a gamma detector so the PSD is not relevant. Best gate determination was done using the measurement with the Cesium source and varying the long gate from 1000 ns up to 3500 ns in steps of 500 and then from 3500 ns until 3900 ns in steps of 100. The data points were plotted in Fig. 5.20 and

the optimal gate was found to be **3600 ns** which corresponds to a resolution of **4.26344**(±**0.00031**) at 662 keV.

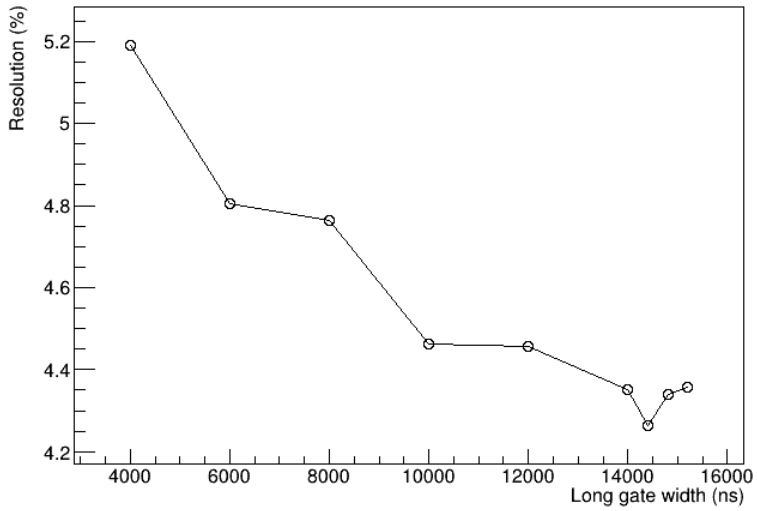

Figure 5.20: SrI_2 : Eu coupled with PMT energy resolution versus long gate width plot (note that the error bars are smaller than the marker size).

Energy Calibration

The energy calibration of the detector was done using several gamma sources mentioned in table 4.7 with the detector coupled to the Hamamatsu R6233 PMT and acquiring the signals with the CAEN DT5725 digitizer, as shown in Fig. 5.19. This was accomplished by doing ∼ **1.5 min** runs with each source and ∼ **5 min** run for background. Afterwards, the background was subtracted from the data, and the different peaks corresponding to different emissions from the sources were fitted with Gaussian functions using the program ***fityk*** [47]. The mean and standard deviations of these peaks were recorded. Finally, the mean was used alongside the known values of the emission energies of the sources obtained from the **Library for gamma and alpha emissions** [33] to fit a straight line as reported in Fig. 5.21.

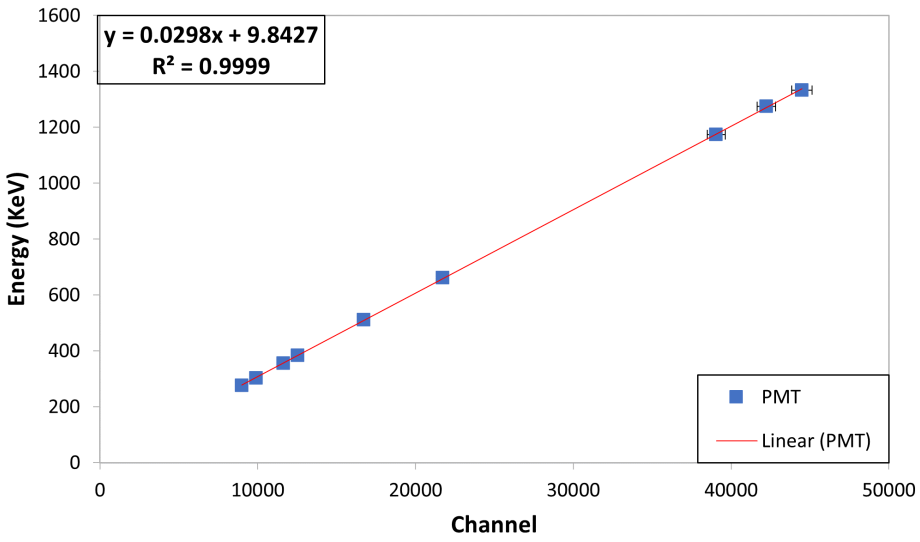

Figure 5.21: SrI_2 : Eu calibration using PMT (R6233).

5.2.2 Coupled to SiPM

Following the measurements using the PMT, the assembly was dismantled and the scintillator was coupled to the SiPM, as demonstrated in Fig.5.22. Since the calibration depends on the readout device, another set of measurements needed to be taken for the SiPM. The system was placed inside the same box due to the geometry of readout board that hindered the ability to properly pack the scintillator as in the case of using PMT.

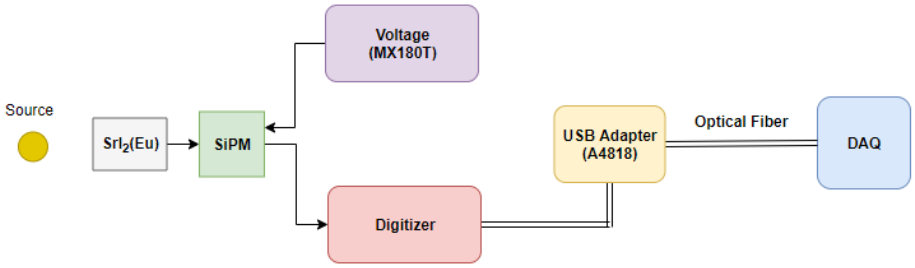

Figure 5.22: Block diagram of the experimental setup of SrI_2 : Eu with SiPM.

Optimal voltage and gate calibration

The Hamamatsu S14161-6050HS-04 SiPM has a breakdown voltage of 38 V. Accordingly, in order to determine its optimal bias voltage, 5 measurements were taken using the ^{137}Cs source starting from 39.5 V up to 41.5 V in steps of 0.5 V (table 5.5). The optimal bias voltage was found to be **41 V**.

Table 5.5: Voltage optimization of SrI_2 : Eu with SiPM

$\mathbf{V_{over}}$**(mV)**	**Centroid**	**FWHM**	**Resolution(%)**
39500	5295.08	548.28	10.35
40000	9808.29	696.93	7.11
40500	15340.02	916.55	5.97
41000	**21984.923**	**1182.01**	**5.38**
41500	29963.16	1613.08	5.38

As for the optimal integration gate, the same test as with the PMT was performed. In this case, starting from 6000 ns until 12000 ns with steps of 800 ns. The best energy resolution was obtained with long gate of **8000** ($\mathbf{5.96459 \pm 0.00039}$) at 662 keV as shown in 5.23.

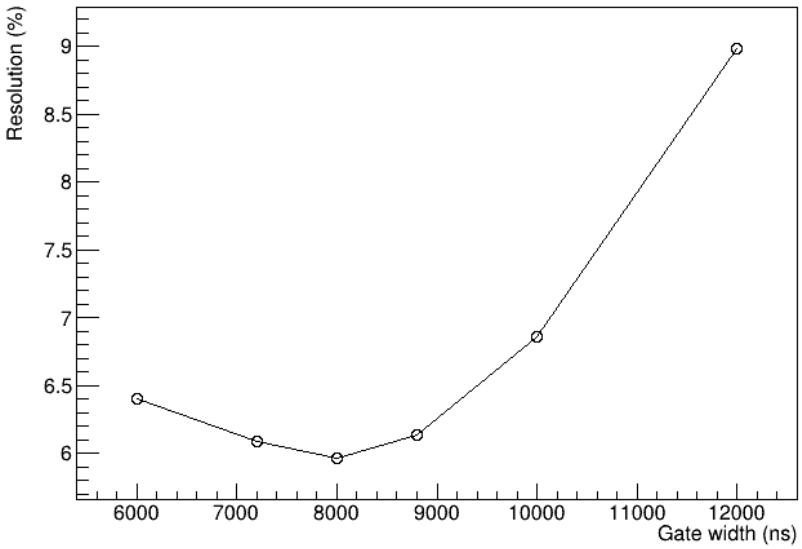

Figure 5.23: SrI_2 : Eu coupled with SiPM energy resolution versus long gate width plot (note that the error bars are smaller than the marker size).

Energy Calibration

In a similar manner to the previous subsection, the calibration of the scintillator with the SiPM was done using the same sources. The detector was coupled to the Hamamatsu S14161-6050HS-04 SiPM and the samples were acquired with the CAEN DT5725 digitizer, as in the case with the PMT. A linear fit was used to determine the calibration constant and its slope. The plot alongside the results can be found in Fig. 5.24.

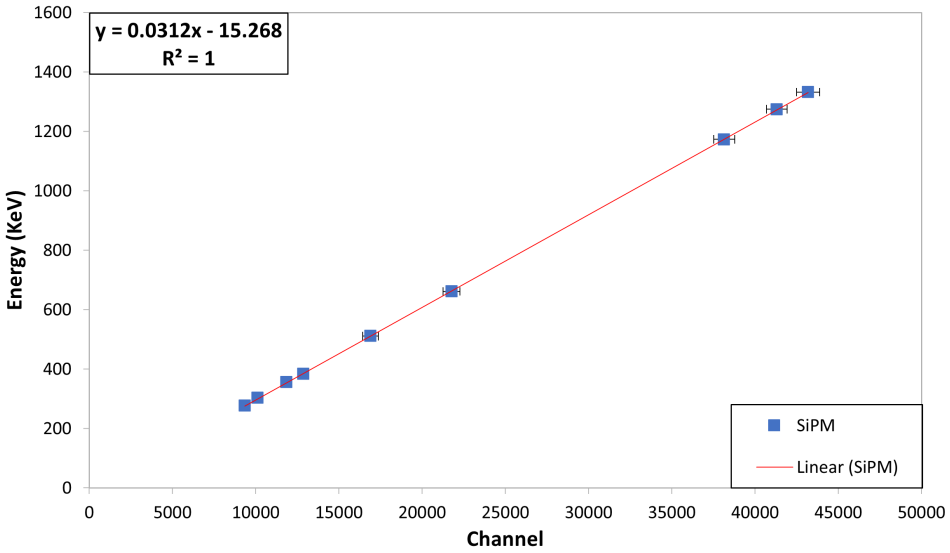

Figure 5.24: SrI_2 : Eu energy calibration using SiPM (S14161-6050HS-04).

A comparison between the waveform using the PMT and the SiPM can be seen in Fig. 5.25.

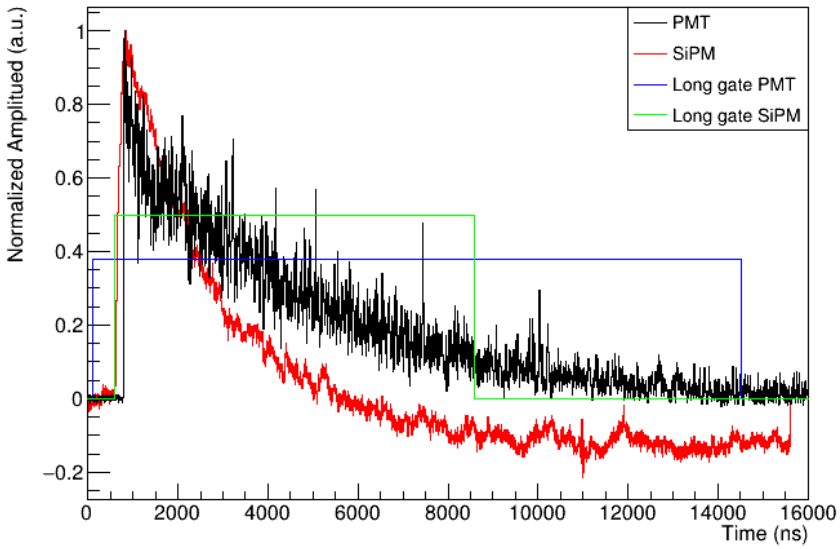

Figure 5.25: SrI_2 : Eu waveform using PMT vs SiPM.

The energy resolutions corresponding to the SrI_2 : Eu coupled to both light detection devices were computed and plotted in Fig. 5.26. A power fit was done for both scenarios and the corresponding equations can be seen in the same figure.

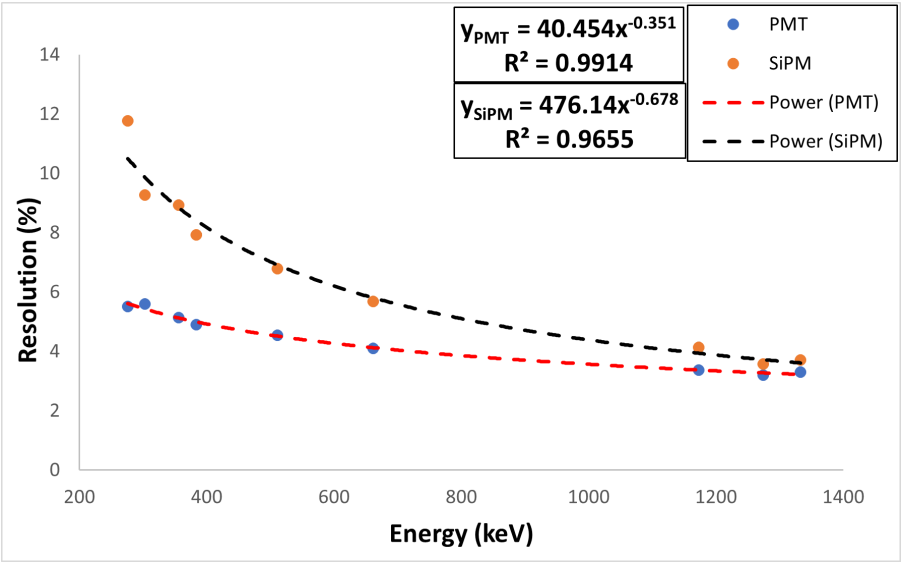

Figure 5.26: SrI_2 : Eu Energy-Resolution curve with power fit for PMT and SiPM.

It is observed that the performance of the setup using the PMT is better than that of SiPM. To be precise, there is a **10.8%** improvement in the resolution for the 662 keV point. This can be a consequence of the light collection efficiency. As the PMT used was substantially larger than the scintillator which meant that the majority of the light produced was collected.

Finally, as mentioned in [12], the energy resolution should, in principle, follow $R = k \times E^{-0.5}$ with k being a constant. However, it can be seen from the experimental fit that the value of power of the energy is either higher or lower than 0.5. This can possibly be due to the several factors of resolution calculation mentioned in [26] such as electron non-proportionality caused by fluctuations of stopping power that were not considered in the uncertainty in resolution for this work as well as other factors

that might cause this deviation. The uncertainty of resolution utilized was obtained by propagation of uncertainty of the mean and FWHM from the Gaussian fit of the energy peak.

5.3 Hybrid detector (EJ-276G coupled with LiBO)

As the LiBO only detects thermal neutrons, and due to its high flexibility, it can be coupled to another scintillator. In the case of this work, it was cut into a circular part and a rectangular part and coupled optically to the EJ-276G plastic scintillator as shown in Fig. 5.27.

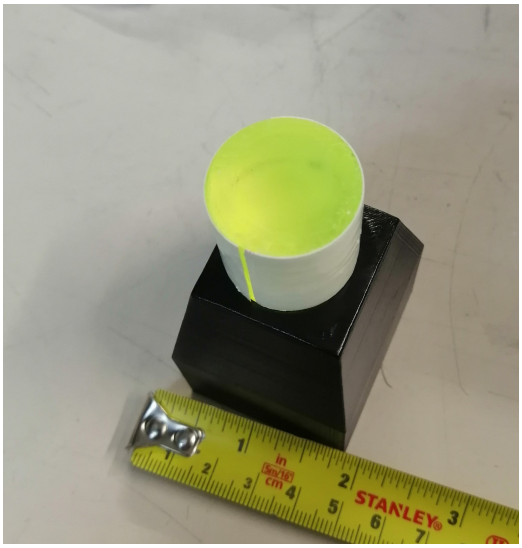

Figure 5.27: EJ-276G coupled optically with LiBO.

The whole setup was then wrapped with black tape and coupled to the PMT for a set of measurements, then disassembled and coupled to an SiPM, then it was placed in a dark box and another set of measurements was taken. The setup with SiPM is intended to be a solution for the DRAGoN project. In this case, it will be connected to the SiPM in a compact robust assembly. A schematic diagram of such assembly can be shown in Fig. 5.28.

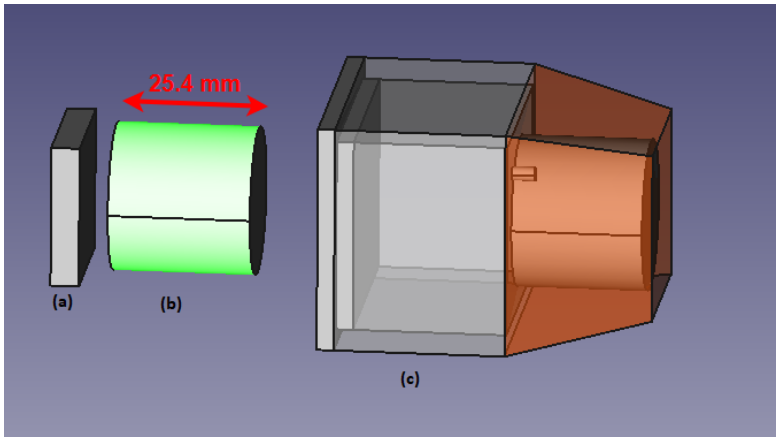

Figure 5.28: Schematic diagram of the Hybrid assembly as a solution for the dragon project.(a)the SiPM coupled to its board.(b)EJ-276G coupled with LiBO.(c)Plastic casing to contain the scinitllator and the readout device.

The goal of the following measurements was to characterize and compare the performance of the EJ-276G scintillator while coupled with the thermal neutron scintillator based on $^{6}Li_{2}^{10}B_{4}O_{7}$ using the

Hamamatsu S14161-6050HS-04 SiPM and comparing to the Hamamatsu H6524 PMT. Since the same SiPM and PMT were utilized in a previous experiment, good estimates of the operating HV for the PMT and the over voltage of the SiPM were possible, and yielded good results. For the PMT, the HV was set to **1350 V** while for the over voltage of the SiPM the best result was set to be **40.7 V**.

5.3.1 Energy Calibration

Following the same procedure as with the EJ-276G, a calibration was made using ^{137}Cs and ^{22}Na. Fig. 5.29 highlights the calibration for the hybrid detector coupled with the SiPM.

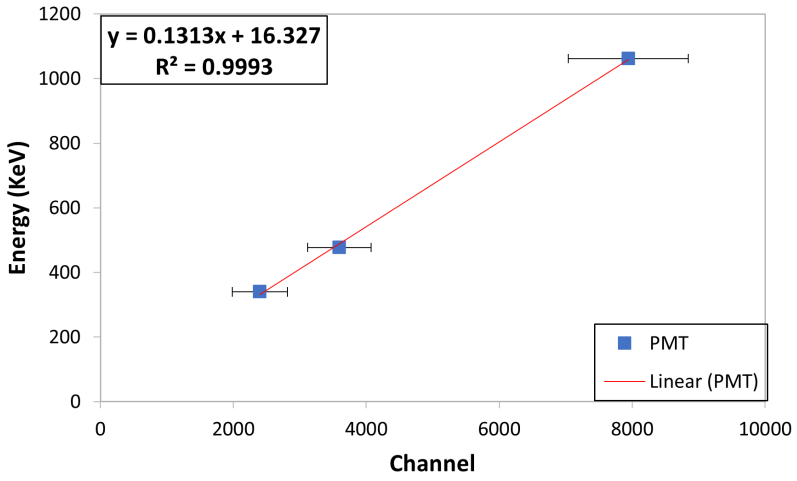

Figure 5.29: Energy Calibration of compound detector with the Hamamatsu S14161-6050HS-04 SiPM.

The gamma spectra of ^{137}Cs and ^{22}Na post calibration can be seen in Fig. 5.30.

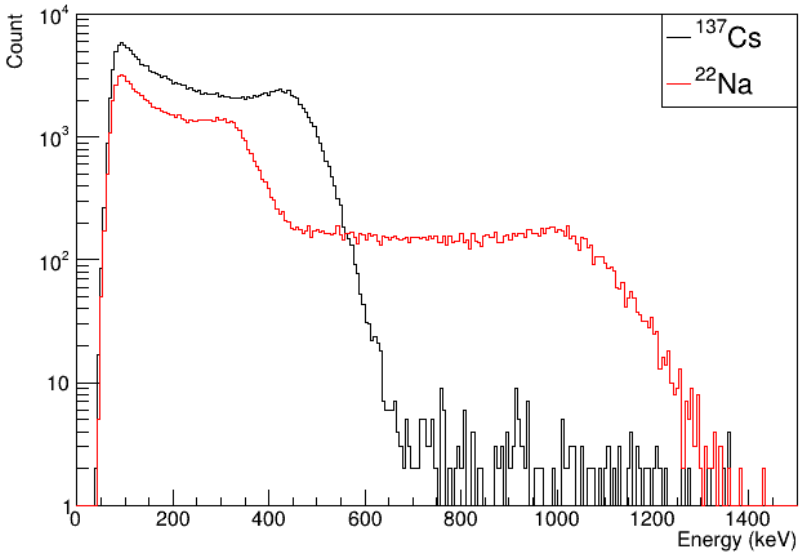

Figure 5.30: Calibrated ^{137}Cs and ^{22}Na spectra.

5.3.2 Energy Resolution

To get an indication of the energy resolution of the hybrid detector using the SiPM, two comparisons were made between the waveforms and the shape of the spectrum using the PMT and the SiPM

Waveform

In order to obtain an idea of the sizes of the integration gates, a comparison between the waveform of the ^{137}Cs spectrum was done as shown in Fig. 5.31. It can be seen that the time needed for the collection of the partial charge and total charge is substantially higher in the case of SiPM than that of the PMT. This is due to the recovery time of the SiPM ($\sim$ 100 ns).

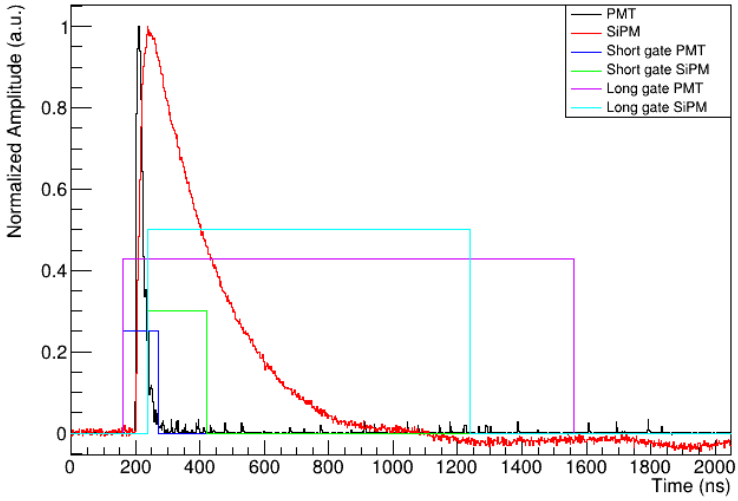

Figure 5.31: Comparison between the waveform of two gamma signals of hybrid detector coupled to PMT and SiPM.

Spectrum shape

To determine which readout device would provide a better resolution in energy, a qualitative analysis of the ^{137}Cs spectrum of PMT and SiPM was made and can be shown in Fig. 5.32. It can be noted that the slope of the spectrum after the Compton edge is much steeper for the SiPM than for the PMT indicating that a better resolution can be obtained using the SiPM.

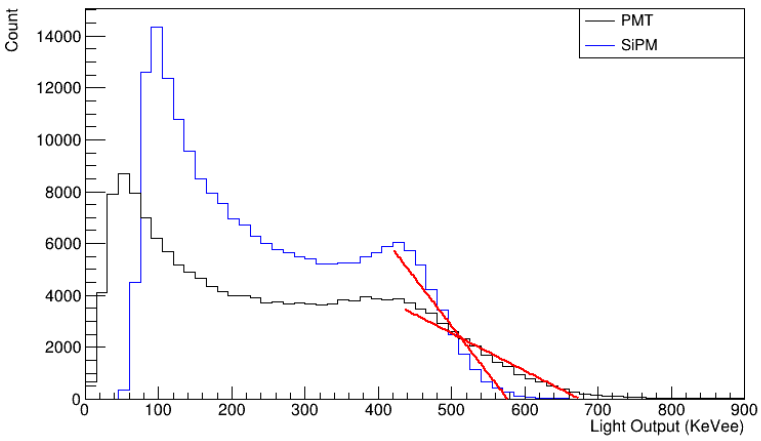

Figure 5.32: Comparison between the spectrum of ^{137}Cs of hybrid detector coupled to PMT and SiPM.

5.3.3 Triple discrimination

One of the merits of this hybrid setup is its ability to discriminate between gamma photons, fast neutrons, and thermal neutrons (Fig. 5.33). To characterize the performance of this setup with the SiPM, several analyses were made. Initially, the optimization of the gates was done to determine the best FoM for the hybrid detector using the SiPM. The optimal gates for the detector using PMT and SiPM can be found int table 5.6. It is notable that the FoM using SiPM was approximately double the value using the PMT. A contributing factor might be the fact that the PMT dimensions were slightly smaller than that of the scintillator (photocathod diameter $\sim$ 19mm while scintillator diameter $\sim$ 25mm) which might have led to a notable amount of light to not be collected by the PMT. As for the SiPM, its dimensions were similar to that of the detector and its characteristics were satisfactory for good discrimination. However, the most important factor was the Photo Detection Efficiency (PDE) and Quantum Efficiency (QE) of the SiPM and PMT respectively. To elaborate, the photo detection efficiency of the SiPM at $\lambda = 420$ nm is $\sim$49% which is much greater than the quantum efficiency of the PMT at the same wavelength which is about 21%.

Table 5.6: Optimal integration gates with corresponding FoM for compound detector coupled to PMT and SiPM

	short gate (ns)	**long gate (ns)**	**FoM**
PMT	**110**	**1400**	**1.09 ± 0.04**
SiPM	**180**	**1000**	**2.07 ± 0.01**

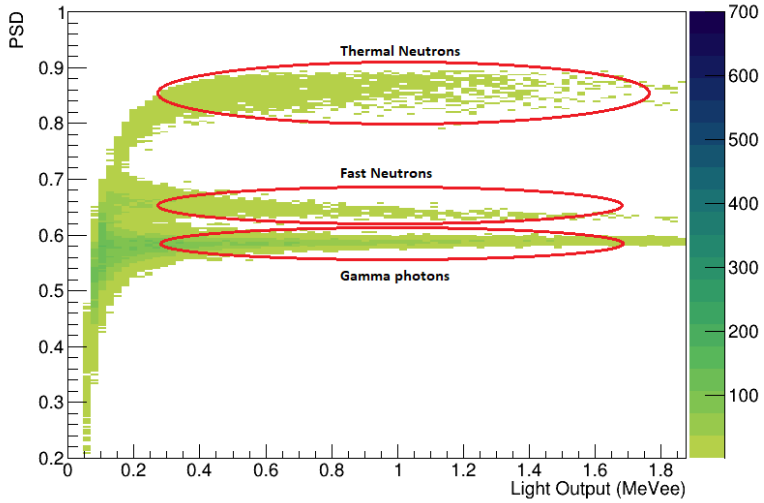

Figure 5.33: Light Output-PSD 2D Histogram of the hybrid detector using SiPM with triple discrimination highlighted.

Triple discrimination from waveform

To further analyze the causes of the performance using the SiPM, the waveforms of gamma photon, fast neutrons and thermal neutrons of the hybrid detector using the SiPM (Fig. 5.34(Left) and PMT (Fig 5.34(right) were plotted. It can be seen that due to the longer time of the SiPM signal, the three different types of particles can be distinguished clearly from each other. However, this means that for a very high neutron rate experiment, pileup will have a pronounced effect on the quality of the gamma and fast neutrons data. Finally, the FoM was computed using multiple light output thresholds (Fig. 5.35) in a similar manner to the process done with the EJ-276G. It can be seen that the same behaviour is observed where the FoM increases as the threshold is set to a higher value.

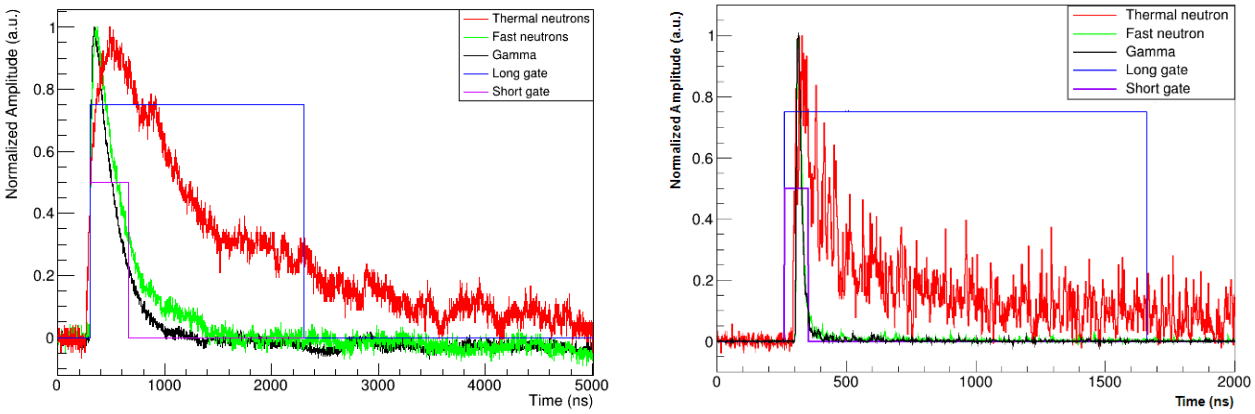

Figure 5.34: Left: Waveforms using SiPM. Right: Waveform using PMT.

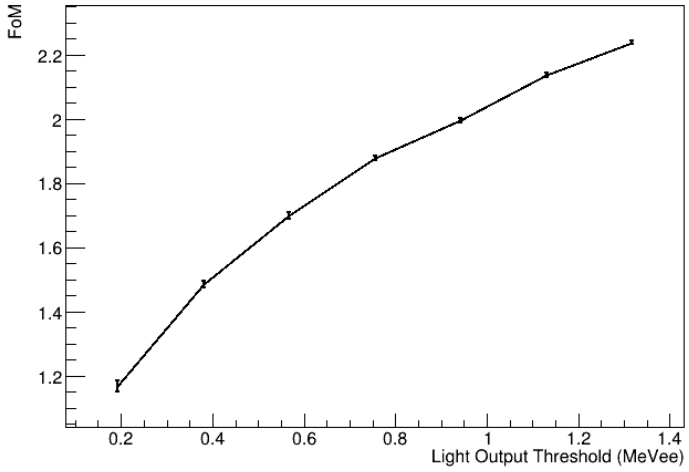

Figure 5.35: FoM Vs Light Output Threshold.

Chapter 6

Conclusion and Outlooks

A study was done in this work to perform a characterization of the EJ-276G scintillator as a candidate to be used for the detection system of the DRAGoN project as part of the radioactivity counter system. The prime goal of the characterization was to determine the proton light output function for the scintillator, gamma efficiency, neutron efficiency, and neutron-gamma discrimination. Optimal values of these features are essential for the use in the DRAGoN project.

The determination of the proton light output function was done by analyzing data with a proton beam used on the EJ-276G scintillator at LABEC accelerator. Different fitting functions were employed to determine which light output function yielded the best reduced chi-squared. The first light output function utilized was the Birk's formula with two different energy loss functions, one using a fit from SRIM data, and the other using the formula from SRIM. Following, a semi-empirical formula from the work [45] was used. This formula yielded much better results and it was used for the other tests.

Subsequently, the neutron-gamma discrimination was determined by finding the optimal integration gates and the best FoM was found to be (0.96 ± 0.06), however, an improvement of the FoM can be achieved using the same integration gates but increasing the threshold of the light output used for the FoM calculations (i.e taking projection at higher energies). To test the results, a GEANT4 simulation was done in which the light output function parameters computed earlier were applied and the neutron spectrum obtained from using a mono-energetic neutron field from LNL. The results showed that the neutron spectra of the simulation and experimental test were similar for higher energy neutrons but deviated for lower energy neutrons, likely due to deviations of fit at lower energy.

Finally, another GEANT4 simulation of the EJ-276G was employed to determine the intrinsic gamma and neutron efficiencies and compare them with the experimental setup. While the experimental gamma efficiency for 662 keV (^{137}Cs) was found to be $\sim 12\%$ with 10% discrepancy from the simulation, the intrinsic neutron efficiency using ^{241}AmBe source with threshold of 300 keV was found to be $\sim 9.4\%$ which was off by $\sim 19\%$ from the simulation.

Another test was performed on a SrI_2(Eu) scintillator to test its performance with an SiPM comparing its performance to PMT in order to explore the possibility of its utilization as a secondary detector for an active target experiment or a gamma detector for the DRAGoN project. The calibration and gate optimization was done for both scenarios and upon comparing the energy resolutions, it was found that using the PMT leads to a better energy resolution by $\sim 10.8\%$ (662 keV), however, this difference becomes smaller at higher energies.

A final test was performed to characterize the new hybrid detector using EJ-276G and LiBO scintillator for triple discrimination using SiPM and comparing to a PMT in order to check its eligibility for the DRAGoN project. The detector was calibrated with the SiPM and PMT and the waveforms and ^{137}Cs spectra were compared. Qualitative analysis concluded that a better energy resolution was

obtainable using the SiPM with respect to the PMT assembly. The neutron-gamma discrimination was studied and the best FoM was found to be (2.0711 ± 0.007) which was approximately double the value obtained using PMT. A further investigation revealed that the waveforms of the SiPM for gamma photons, fast, and thermal neutrons notably varied in shape which enabled better discrimination using the PSD.

In conclusion, the EJ-276G scintillator was tested and characterized for its use in the DRAGoN project and new light output function parameters were obtained. The fitting could be improved by including more points and using more sophisticated minimization method. Additionally, the neutron-gamma discrimination could be improved by having a larger size scintillator. Following, study of the energy resolution of the $SrI_2 : Eu$ scitnillator was performed. Although preliminary studies conclude that replacing the currently used $NaI : Tl$ or $LaBr_3 : Ce$ scintillators with $SrI_2 : Eu$ is not advised as the performance and available sizes are inferior to the other detectors of similar price, bigger size $SrI_2 : Eu$ and performing additional tests might change that fact as the $SrI_2 : Eu$ does not have the activity problem of the $LaBr_3 : Ce$. Finally, the new hybrid detector was tested and provided a decent triple discrimination, however, under high gamma irradiation it maintained the thermal neutron-gamma discrimination while the fast neutron-gamma discrimination drastically decreased. A pileup recognition algorithm and a bigger size scintillator might improve these result.

Bibliography

[1] Special Nuclear Material [Internet]. NRC Web. 2021 [cited 25 April 2022]. Available from: https://www.nrc.gov/materials/sp-nucmaterials.html

[2] Marques L, Vale A, Vaz P. State-of-the-Art Mobile Radiation Detection Systems for Different Scenarios. Sensors. 2021;21(4):1051.

[3] Incident and Trafficking Database (ITDB) — IAEA [Internet]. Iaea.org. 2021 [cited 23 April 2022]. Available from: https://www.iaea.org/resources/databases/itdb

[4] Neutron Technique in civil security applications (presentation by Sandra Moretto) [Internet]. [cited 25 March 2022]. Available from: https://agenda.infn.it/event/17273/contributions/96009/.

[5] Brunelli, D., Pino, F., Fontana, C.L., Pancheri, L., & Moretto, S. (2020). DRAGoN: Drone for Radiation detection of Gammas and Neutrons. 2020 IEEE Sensors, 1-4.

[6] S.Moretto, F.E. Pino Andrades , J. Delgado, C.L. Fontana, D. Fabris, G. Nebbia, M. Turcato, D. Brunelli, L. Pancheri, A. Quaranta: UAV prototype for localization and identification of radioactive contamination and emitters. 2021

[7] Gianfranco Prete, Alberto Andrighetto, Juan Esposito, Pierfrancesco Mastinu, Jeffery Wyss: The SPES project: a second generation ISOL facility. Physics Procedia 26 (2012) 274 – 283.

[8] User S. Home - Eljen Technology [Internet]. Eljentechnology.com. 2021 [cited June 2022]. Available from: https://eljentechnology.com/

[9] Home [Internet]. Hamamatsu.com. 2022 [cited 16 May 2022]. Available from: https://www.hamamatsu.com/eu/en/index.html

[10] J. C. Delgado, F. Pino, S. M. Carturan, M. Polo, G. Mantovani, D. Fabris, A. Quaranta, S. Moretto: Flexible composite thermal neutron scintillator based on fully enriched Lithium Tetraborate. LNL Annual Report Contributions (2021). Available from: https://www1.lnl.infn.it/ annrep/

[11] CAEN - Tools for Discovery [Internet]. CAEN - Tools for Discovery. 2022 [cited 20 July 2022]. Available from: https://www.caen.it/.

[12] Knoll G. Radiation detection and measurement. 4th ed. New York: Wiley; 1979.

[13] Birks J. B. The Theory and Practice of Scintillation Counting. Pergamon Press Ltd., 1st Edition, 1964.

[14] J. B. Birks: Scintillations from Organic Crystals: Specific Fluorescence and Relative Response to Different Radiations. 1951 Proc. Phys. Soc. A 64 874.

[15] Pino F. Development of Innovative Technology for Detection and Identification of Radioactive Materials. PhD Thesis, Univerity of Padova; 2014.

[16] Stefaan Tavernier Experimental Techniques in Nuclear and Particle Physics. Springer Berlin, Heidelberg 2010. 978-3-642-42602-5.

[17] SensL. Introduction to SiPM. 2017.

[18] AdvanSiD Introduction to SiPMs. Rev2 -09.2014.

[19] Pino F, Delgado J, Mantovani G, Pancheri L, Fabris D, Fontana C et al. Novel neutron detector assembly based on SiPM readout to be coupled with the Active Target for SPES.

[20] Delgado J. Design and characterization of the neutron-gamma detection module of the DRAGON project. Master Thesis, University of Padova; 2021.

[21] Fontana C, Carnera A, Lunardon M, Pino F, Sada C, Soramel F et al. A distributed data acquisition system for nuclear detectors. International Journal of Modern Physics: Conference Series. 2018;48:1860118.

[22] B. Mauss, P. Morfouace, T. Roger, J. Pancin, G.F. Grinyer, et al.. Commissioning of the ACtive TARget and Time Projection Chamber (ACTAR TPC). Nuclear Instruments and Methods in Physics Research Section A: Accelerators, Spectrometers, Detectors and Associated Equipment, Elsevier, 2019, 940, pp.498-504. ff10.1016/j.nima.2019.06.067ff. ffhal-02187899.

[23] Redding, Caleb J., "An Investigation of Plastic Scintillators for Radiation Sensing and Mechanical Applications. " PhD diss., University of Tennessee, 2021. Available from https://trace.tennessee.edu/utk_graddiss/6757.

[24] S. Takeuchia,, T. Motobayashi, Y. Togano, M. Matsushita, N. Aoi, K. Demichi, H. Hasegawa, H. Murakami DALI2: A NaI(Tl) detector array for measurements of γ rays from fast nuclei. Nuclear Instruments and Methods in Physics Research A 763 (2014) 596–603.

[25] User S. EJ-276 - Pulse Shape Discrimination Plastic Scintillator - Eljen Technology [Internet]. Eljentechnology.com. 2021 [cited 20 July 2022]. Available from: https://eljentechnology.com/products/plastic-scintillators/ej-276.

[26] N.J. Cherepy, S.A. Payne, S.J. Asztalos, G. Hull, J.D. Kuntz, T. Niedermayr, S. Pimputkar, J.J. Roberts, R.D. Sanner, T.M. Tillotson, E. van Loef, C.M. Wilson, K.S. Shah, U.N. Roy, R. Hawrami, A. Burger, L.A. Boatner, W.-S. Choong and W.W. Moses: Scintillators with Potential to Supersede Lanthanum Bromide. 2018

[27] Home [Internet]. advatech-uk.co.uk. 2022 [cited 20 August 2022]. Available from: https://www.advatech-uk.co.uk

[28] Leo W. Techniques for nuclear and particle physics experiments. 2nd ed. Berlin: Springer-Verlag; 1994.

[29] S.M Carturan et al., NIM A vol 925, 1, pag. 109-115, 2019.

[30] Aim TTi - Measurably better value [Internet]. Aim TTi - Measurably better value. 2022 [cited 20 August 2022]. Available from: https://www.aimtti.com/.

[31] CAEN User Manual UM5960 CoMPASS Multiparametric DAQ Software for Physics Applications. Rev 18 15 February 2022.

[32] Cester D. Materials, instrumentation and techniques for the detection of Special Nuclear Material and Radioactive Sources: EU project MODES SNM. PhD Thesis, University of Padova.

[33] Library for gamma and alpha emissions [Internet]. http://www.nucleide.org/Laraweb/index.php. [cited 20 August 2022] 2022.

[34] M. Chiaria , S. Barone, A. Bombini, G. Calzolai, L. Carraresi, L. Castelli, C. Czelusniak, M. E. Fedi, N. Gelli, F. Giambi, F. Giardi, L. Giuntini, S. Lagomarsino, L. Liccioli, F. Lucarelli, M. Manetti, M. Massi, A. Mazzinghi, S. Nava, P. Ottanelli, S. Sciortino, C. Ruberto, L. Sodi, F. Taccetti, P. A. Mandò: LABEC, the INFN ion beam laboratory of nuclear techniques for environment and cultural heritage. Eur. Phys. J. Plus (2021) 136:472.

[35] A. Giaz, N. Blasi, C. Boiano, S. Brambilla, F. Camera, C. Cattadori, S. Ceruti, F. Gramegna, T. Marchi, I. Mattei, A. Mentana, B. Million, L. Pellegri, M. Rebai, S. Riboldi, F. Salamida, M. Tardocchi: Fast neutron measurements with ^{7}Li and ^{6}Li enriched CLYC scintillators Nuclear Instruments and Methods in Physics Research A. 2016.

[36] N. Metropolis THE BEGINNING of the MONTE CARL0 METHOD. Los Alamos Science Special Issue 1987.

[37] Alex F Bielajew Fundamentals of the Monte Carlo method for neutral and charged particle transport. February 11, 2000.

[38] Agostinelli S. et al. Geant4 a simulation toolkit. Nuclear Instruments and Methods in Physics Research A, 506:250-303, 2003.

[39] Grodzicka-Kobylka M, Szczesniak T, Moszynski M, Brylew K, Swiderski L, Valiente-Dobon J et al. Fast neutron and gamma ray pulse shape discrimination in EJ-276 and EJ-276G plastic scintillators. Journal of Instrumentation. 2020;15(03):P03030-P03030.

[40] Reference Physics Lists, Geant4 Simulation Toolkit [Internet]. https://geant4.web.cern.ch/. 2022 [cited 25 July 2022]. Available from: https://geant4.web.cern.ch/node/155.

[41] Can Liao, Haori Yang Pulse shape discrimination using EJ-299-33 plastic scintillator coupled with a Silicon Photomultiplier array. Nuclear Instruments and Methods in Physics Research A 789 (2015) 150–157.

[42] Stopping and Range of Ions in Matter (SRIM) [Internet]. http://www.srim.org. 2022 [cited 24 June 2022] Availavle from: http://www.srim.org/SRIM/SRIM2011.htm.

[43] S. Nyibule, J. Tõke, E. Henry, W.U. Schröder, L. Acosta, L. Auditore, G. Cardella, E. De Filippo, L. Francalanza, S. Gianì, T. Minniti, E. Morgana, E.V. Pagano, S. Pirrone, G. Politi, L. Quattrocchi, P. Russotto, A. Trifirò, M. Trimarchi: Birks' scaling of the particle light output functions for the EJ 299-33 plastic scintillator. Nuclear Instruments and Methods in Physics Research A 768 (2014) 141–145.

[44] Table of Isotopes 8th edition Richard B. Firestone, S.Y. Frank Chu, Coral M. Baglin. Available from: https://application.wiley-vch.de/books/info/0-471-35633-6/toi99/toi.htm

[45] F. Pino, L. Stevanato, D Cester, G. Nebbia, L. Sajo-Bohus, G. Viesti The light output and the detection efficiency of the liquid scintillator EJ-309. Applied Radiation and Isotopes 89 (2014) 79–84.

[46] Chris C. Lawrence, Michael Febbraro, Thomas N. Massey, Marek Flaska, F.D. Becchetti, Sara A. Pozzi Neutron response characterization for an EJ299-33 plastic scintillation detector. Nuclear Instruments and Methods in Physics Research A 759 (2014) 16–22.

[47] Fityk User Manual [Internet]. https://fityk.nieto.pl 2022 [cited 25 August 2022] Available from: https://fityk.nieto.pl/fityk-manual.html

.